ALMA MATER STUDIORUM
UNIVERSITÀ DI BOLOGNA

SCUOLA DI INGEGNERIA E ARCHITETTURA
- SEDE DI FORLÌ -

Corso di Laurea in Ingegneria Aerospaziale
Classe: LM-20

TESI DI LAUREA IN
FLUIDODINAMICA LM

A numerical study of turbulent Rayleigh-Bénard convection

Candidato:
Riccardo Togni
Matricola 0000641037

Relatore:
Prof. Elisabetta De Angelis

Correlatore:
Prof. Andrea Cimarelli

Anno Accademico 2012-2013
Sessione II^a

Abstract

Il flusso di Rayleigh-Bénard, costituito da un fluido racchiuso fra due pareti a diversa temperatura, rappresenta il paradigma della convezione termica. In natura e nelle applicazioni industriali, il moto convettivo avviene principalmente in regime turbolento, rivelando un fenomeno estremamente complesso. L'obiettivo principale di questo elaborato di tesi consiste nell'isolare e descrivere gli aspetti salienti di un flusso turbolento di Rayleigh-Bénard. L'analisi è applicata a dati ottenuti da tre simulazioni numeriche dirette effettuate allo stesso numero di Rayleigh ($Ra \approx 10^5$) e a numeri di Prandtl differenti ($Pr = 0.7, 2, 7$). Sulla base di alcune statistiche a singolo punto, vengono definite nel flusso tre regioni caratteritiche: il *bulk* al centro della cella, lo strato limite termico e quello viscoso in prossimità delle pareti. Grazie all'analisi dei campi istantanei e delle correlazioni spaziali a due punti, sono state poi individuate due strutture fondamentali della convezione turbolenta: le piume termiche e la circolazione a grande scala. L'equazione generalizzata di Kolmogorov, introdotta nell'ultima parte della trattazione, permette di approcciare il problema nella sua complessità, visualizzando come l'energia cinetica viene immessa, si distribuisce e viene dissipata sia nello spazio fisico, sia in quello delle scale turbolente. L'immagine che emerge dall'analisi complessiva è quella di un flusso del tutto simile a una macchina termica. L'energia cinetica viene prodotta nel *bulk*, considerato il motore del flusso, e da qui fluisce verso le pareti, dove viene infine dissipata.

A mio padre, Agostino.

Contents

Chapter 1

Introductory concepts

Thermally driven turbulence plays a major role in several natural and industrial processes. It occurs in Earth's outer core, atmosphere and oceans. A clear example is seen in stratocumulus clouds over the oceans, where a dominant feature is a polygonal pattern of light areas surrounded by darker boundaries (see Figure 1.1(a)). Covering vast areas of the ocean at any given time, such cloud systems play a significant role in regulating the amount of sunlight that reaches the planet [12]. In the astrophysical context turbulent convection is seen in the outer layer of the Sun (see Figure 1.1(b)) and in the atmosphere of giant planets. Furthermore thermally driven turbulence is of utmost importance in industrial applications ranging from miniaturized heat exchangers for cooling of electronic components to large scale power plants. Convective motion is also important in metal-production processes controlling the growth of crystals from the melt.

The processes mentioned in the previous paragraph are extremely complex. Even though the fluid motion is simply triggered by buoyancy due to density variations, occurring in the presence of a gravitational field, turbulent convection is coupled with other physical processes such as Coriolis force, electromagnetic fields and chemical reactions. Moreover every system has distinct and complex boundary conditions.

1.1 Turbulent Rayleigh-Bénard convection

Rayleigh-Bénard convection is the idealized system to study properties of thermal convection (see Figure 1.2). It consists of a fluid layer heated from below and cooled from above in a vertically bounded domain. The horizontal plates at the top and at

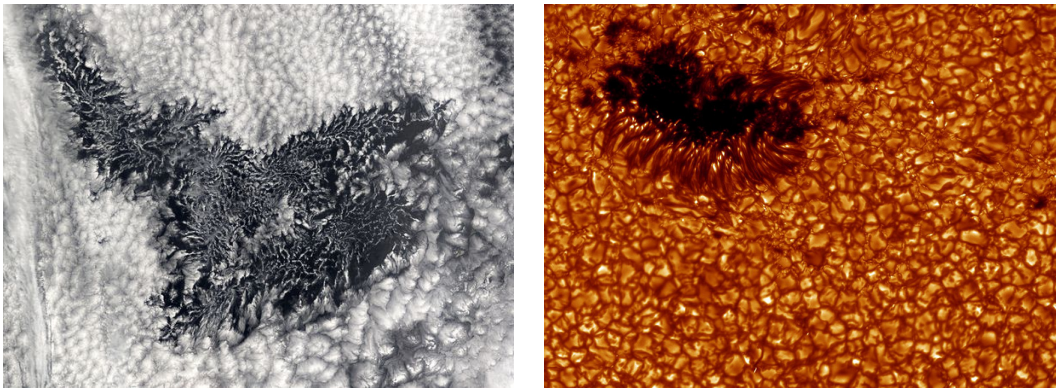

(a) (b)

Figure 1.1: (a) Convective cells in a cloud system over the Pacific Ocean. Satellite image courtesy of NASA. (b) Granules and a sunspot observed in the Sun's photosphere on 8 August 2003 by Göran Scharmer and Kai Langhans with the Swedish 1-m Solar Telescope operated by the Royal Swedish Academy of Sciences. (Illustration: RSAS)

the bottom are kept at constant temperatures, T_{top} and T_{bottom}, respectively, such that $\Delta T = T_{bottom} - T_{top}$ is positive. The fluid motion starts when buoyancy force overcomes viscous drag and thermal diffusion. These dynamics can be summarized in two non-dimensional parameters, the Rayleigh number Ra and the Prandtl number Pr, respectively defined as

$$Ra = \frac{g\alpha\Delta T H^3}{\nu\kappa}, \qquad Pr = \frac{\nu}{\kappa}, \tag{1.1}$$

with g the gravity acceleration, α the thermal expansion coefficient, H the height of the fluid layer, ν the kinematic viscosity and κ the thermal diffusivity of the fluid. The Rayleigh number quantifies the relative importance of the driving effect due to buoyancy to the dampening effect due to kinematic viscosity and thermal diffusivity. The Prandtl number compares the momentum transport to thermal energy transport. A third flow parameter is the aspect-ratio of the cell Γ, defined as

$$\Gamma = \frac{L}{H}, \tag{1.2}$$

where L is a characteristic horizontal scale such as the diameter of a cylindrical cell or the lateral size of a rectangular cell.

Rayleigh-Bénard convection develops in response to parameters Ra, Pr e Γ just

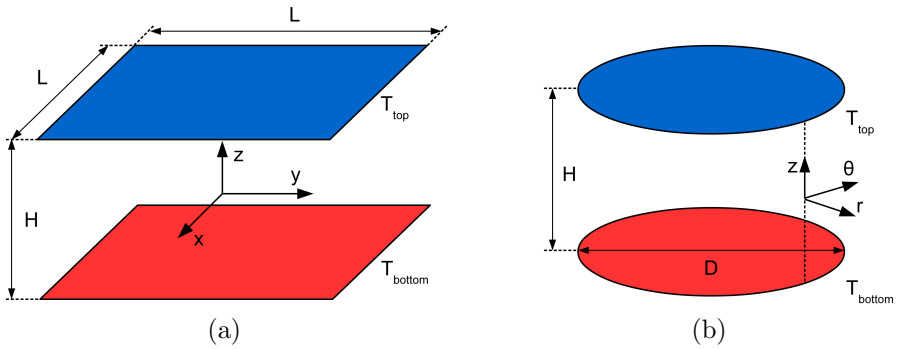

(a) (b)

Figure 1.2: The typical Rayleigh-Bénard convection setups as a rectangular cell (a) or a cylindrical cell (b).

defined. The resultant flow is characterized by a transport of momentum and thermal energy which can be quantified, respectively, by the Reynolds Re and the Nusselt number Nu, defined as

$$Re = \frac{UH}{\nu}, \qquad Nu = \frac{\phi}{\kappa(\Delta T/H)}, \tag{1.3}$$

where U is a characteristic velocity and ϕ is the heat flux through the top and the bottom walls. The Reynolds number quantifies the relative importance of inertial and viscous forces whereas the Nusselt number measures the competition of convective thermal transport in comparison with conduction. Using the *free-fall* velocity $U_f = \sqrt{g\alpha\Delta TH}$ as a characteristic velocity, Re can be rewritten as

$$Re = \sqrt{\frac{Ra}{Pr}}. \tag{1.4}$$

therefore for a fixed Γ, the flow regime depends on the ratio of Ra to Pr.

For a given fluid in a given cell i.e. fixed Pr and Γ, the Rayleigh-Bénard convection is driven by Ra only, assuming that the fluid properties do not change with temperature. When Ra is small enough there is no fluid motion and thermal flux is purely conductive. Laminar convection arises only when Ra is greater than some critical value Ra_c, which for a lateral unbounded Rayleigh-Bérnard is about 1708 [1]. At the bifurcation from the state of rest, a steady pattern of parallel roll cells occurs. However when Ra is sufficiently high, the flow first becomes chaotic in time, then for $Ra > Ra_t$ the spatial periodicity is lost and fully developed turbulence arises.

Turbulent Rayleigh-Bénard convection is a fascinating example of self-organized system. The flow behaves like a "machine", meaning that it presents different working parts, each serving a different function [15]. Two thermal boundary layers of thickness much less than H adhere to the horizontal walls, as the local Rayleigh number does not exceed the critical value. Far enough from the wall, parts of the thermal boundary layer detach permanently and move into the bulk of the cell, driven by buoyancy forces. These coherent structures, called *thermal plumes*, group together and give life to a large-scale circulation which, in turn, generates two viscous boundary layers, as shown in Figure 1.3.

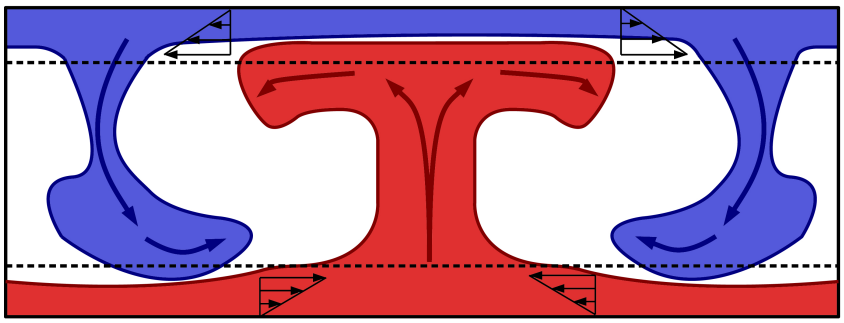

Figure 1.3: Sketch of turbulent Rayleigh-Bénard convection: hot (red) and cold (blue) plumes detach from the thermal boundary layers, move into the bulk and give life to a large scale circulation. The dashed line indicates the edge of a viscous boundary layer.

In this thesis, two strategies to isolate features of turbulent Rayleigh-Bénard convection are adopted. The first classical approach consists of analyzing single-point statistics and two-point correlations. The simplest single-point statistics (mean and variance) allow the identification of different regions in the flow, such as the beforementioned thermal and viscous boundary layers, whereas to display mechanisms of energy production, transport and dissipation occurring in the space domain, a more powerful single-point statistic, the turbulent kinetic energy budget, is required. Furthermore, two-point correlations are introduced to measure the characteristic lengths of plumes. Turbulence is a multi-scale phenomenon, which means that in a generic point of the space domain, flow structures (i.e. eddies) of various sizes coexist. The turbulent kinetic energy equation gives a picture of turbulence only at the largest scale, therefore it is insufficient to describe completely the dynamics of the phenomenon. The analysis of a scale-by-scale budget for the turbulent fluctuations is the core of the second approach. This equation describes how the energy associated with

a specific scale of motion is transferred through the spectrum of scales and, simultaneously, how the same scale of motion exchanges energy with a properly defined spatial flux.

Both approaches are applied to the results provided by direct numerical simulations (DNS) of a rectangular $\Gamma = 8$ domain at $Ra \approx 10^5$ and $Pr = \{0.7, 2, 7\}$, with periodic boundary conditions in the horizontal directions x and y. Direct numerical simulation refers to solving the Navier-Stokes equations numerically by resolving all the scales of turbulence down to the smallest one. Each DNS presented here is obtained by solving the governing equations in a non-dimensional form, hence it corresponds to a family of experimental realizations performed at the same Ra, Pr and Γ.

In Table 1.1 three experimental realizations, one for each DNS, are reported. By imposing the fluid type and the operating mean temperature (in this case, 293 K), the thermal expansion coefficient α, the kinematic viscosity ν, the thermal diffusivity κ and, therefore, the Prandtl number, are defined. Furthermore, the temperature difference across the top and bottom plates ΔT and the height of the cell H are chosen to univocally define the Rayleigh number.

Fluid	$\alpha \quad K^{-1}$	$\nu \quad m^2 \cdot s^{-1}$	$\kappa \quad m^2 \cdot s^{-1}$	$\Delta T \quad K$	$H \quad mm$
Air	$3.4 \cdot 10^{-3}$	$1.52 \cdot 10^{-6}$	$2.12 \cdot 10^{-7}$	10	54
Liquid ammonia	$1.5 \cdot 10^{-3}$	$3.62 \cdot 10^{-7}$	$1.82 \cdot 10^{-7}$	10	4
Water	$2.1 \cdot 10^{-4}$	$1.00 \cdot 10^{-6}$	$1.44 \cdot 10^{-7}$	10	11

Table 1.1: Three different experimental setups. The first, the second and the third lines correspond to the $Pr = 0.7$, $Pr = 2$, $Pr = 7$ simulations, respectively. The fluid properties are evaluated at 293 K.

1.2 State of the art

Convective turbulence remains the subject of many studies, as it is very commonly found in nature as well as in industry. Two topics in particular have received a lot of attention in the last years. The first one concerns the scaling properties of thermal transport, that is how the Nusselt number depends on Rayleigh and Prandtl numbers. The second topic of interest is represented by the effect of buoyancy forces on statistical properties of turbulent fluctuations.

It has already been noticed that the Nusselt number is the ratio of convective to conductive heat transfer. Despite an extensive investigation in the past due to the importance of heat transfer and mixing in engineering problems, the dependence of Nu on Ra and Pr is still not clear and a unifying theory for $Nu = f(Ra, Pr)$ presents some discrepancies with experimental results [11].

One of the oldest models for predicting the Nusselt number as a function of the Rayleigh number goes back to Malkus' marginal-stability theory of 1954. It assumed that the thermal boundary layer thickness adjusts itself so as the local Rayleigh number, based on the thermal boundary layer thickness, reaches the critical value $Ra_c = O(10^3)$. This gives the power law

$$Nu \sim Ra^{1/3} \tag{1.5}$$

The later investigations by Castaing *et al.* in 1989 [5] with higher accuracy in helium ($Pr = 1$ and $Ra \geq 10^6$) and by Ciliberto in 1993 [7] ($Ra < 10^6$), show another scaling

$$Nu \sim Ra^{2/7} \tag{1.6}$$

Several theoretical interpretations have been offered for this power law but the one that seems most consistent with its occurrence is by Shraiman and Siggia in 1990 [27]. This theory is based on the relevant dynamical role played by the large-scale circulation in turbulent Rayleigh-Bénard convection. The onset of a mean flow is due to plumes rising from the unstable boundary layer. On the other hand, the mean flow generates a viscous boundary layer which, in turn, controls the thickness of the thermal boundary layer. Without providing a rigorous demonstration of the power law, it is enough to consider that the most important assumption in the Shraiman and Siggia theory is that all kinetic energy dissipation is constrained inside the viscous boundary layers [4].

In the last few years, given the increasing precision of experimental and numerical data, it became clear that none of the theories for $Nu(Ra, Pr)$ developed in the past could offer a unifying view, accounting for all data. Therefore in a series of papers, Grossmann and Lohse tried to develop a unifying theory to account for both $Nu = (Ra, Pr)$ and $Re = (Ra, Pr)$ over wide parameter ranges, assuming thermal and kinetic dissipation in the boundary layers and the bulk [3]. They composed a

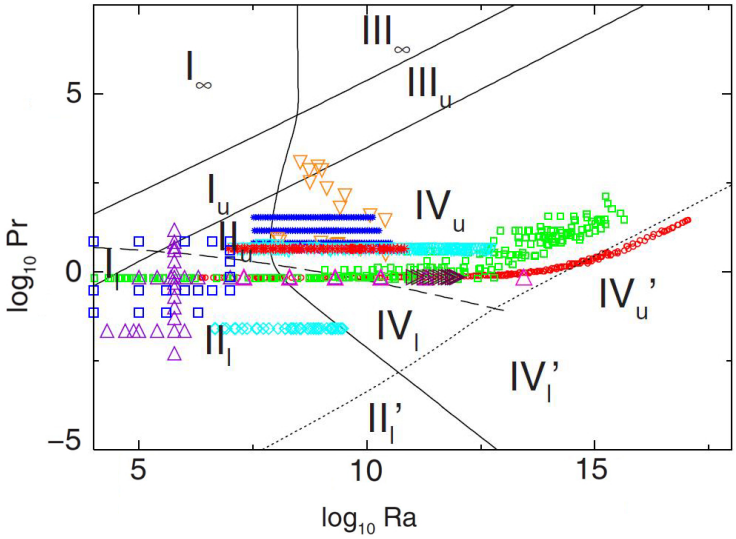

Figure 1.4: Phase diagram in $Ra - Pr$ plane indicating the different turbulent regimes in Grossmann and Lohse theory. The data points indicate where Nu has been measured or numerically calculated. This figure is adapted from [2], where more details can be found.

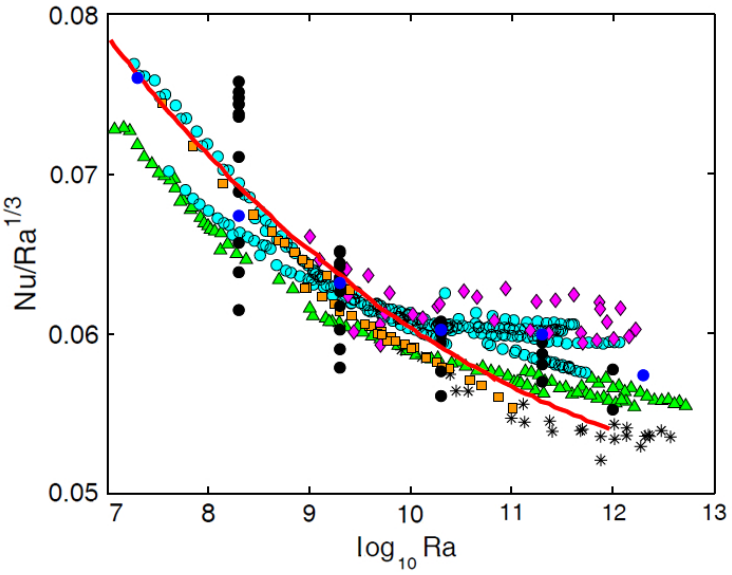

Figure 1.5: Heat transport as a function of Rayleigh number. The red solid line represents the curve obtained from the Grossman and Lohse theory. The data points indicate several experimental results. This figure is adapted from [6], where more details can be found.

phase diagram with different power laws for the different regions of Ra and Pr. As an instance, for $Ra = 10^5$ and $Pr = 7$ the Nusselt number is located in the area

I_l as can be seen in Figure 1.4. Moreover, the scaling proposed for this particular regime is $Nu \sim Ra^{1/4}Pr^{1/8}$ [13].

In Figure 1.5 the results of several experiments in cylindrical cells are summarized in a compensated plot $NuRa^{-1/3}$ versus Ra. The first impression is that the data scatter, however, it should be considered that these results have been obtained for different experimental conditions (different materials for the walls), different aspect-ratios ($0.23 \leq \Gamma \leq 20$) and different systems of thermal insulation. Taking into account all these factors, we can reasonably conclude that the Grossmann and Lohse theory fits quite well the results. Nevertheless, it is yet an open point if further effects exists that may influence the flow and thus the heat transfer measurements [6].

Investigating the effect of buoyancy forces on the statistical properties of turbulent fluctuations represents another major challenge nowadays. Turbulent fluctuations can be quantified by introducing velocity and temperature differences measured at the same time t and at two positions separated by a displacement vector r_i, defined respectively as

$$\delta u_i(x_i, r_i) = u_i(x_i + r_i/2, t) - u_i(x_i - r_i/2, t), \tag{1.7a}$$

$$\delta\theta(x_i, r_i) = \theta(x_i + r_i/2, t) - \theta(x_i - r_i/2, t), \tag{1.7b}$$

where $i = x, y, z$, x_i is the position vector in the geometric domain, $u_i(x, y, z, t)$ and $\theta(x, y, z, t)$ are respectively the fluctuating velocity and temperature fields. Now, we can introduce a fundamental statistic for the fluctuating increments of velocity and temperature (for more details see Section 3.2), defined respectively as

$$\left\langle \delta u^2 \right\rangle (x_i, r_i) = \langle \delta u_i(x_i, r_i)\delta u_i(x_i, r_i) \rangle \tag{1.8a}$$

$$\left\langle \delta\theta^2 \right\rangle (x_i, r_i) = \langle \delta\theta(x_i, r_i)\delta\theta(x_i, r_i) \rangle \tag{1.8b}$$

where $\langle\cdot\rangle$ denotes the ensemble average, $\langle \delta u^2 \rangle$ and $\langle \delta\theta^2 \rangle$ are respectively the *second-order structure functions* for velocity and temperature and quantifies the amount of kinetic and thermal energy of a turbulent structure or eddy of scale $r = \sqrt{r_i r_i}$ located at the point x_i of the space domain.

Under certain conditions, turbulence can be assumed homogeneous and isotropic, consequently $\langle \delta\beta^2 \rangle (x_i, r_i) = \langle \delta\beta^2 \rangle (r)$, where β is a generic variable. In the case of Rayleigh-Bénard convection only the horizontal planes form a statistical ho-

mogeneous and isotropic space while the presence of the walls induces anisotropy and inhomogeneity in the vertical direction. Hence, $\langle \delta\beta^2 \rangle = \langle \delta\beta^2 \rangle (r, z)$, where r is an increment lying in the horizontal planes. In turbulent convection, temperature variations result in a buoyancy force that drives the fluid motion, and temperature is an active scalar. Nevertheless, at small scales r, temperature behaves like a passive scalar and buoyancy is negligible; in this case, it can be demonstrated by dimensional analysis, that the following scaling laws exist

$$\left\langle \delta u^2 \right\rangle (r) \sim \langle \epsilon \rangle^{2/3} r^{2/3}, \tag{1.9a}$$

$$\left\langle \delta \theta^2 \right\rangle (r) \sim \langle \chi \rangle \langle \epsilon \rangle^{-1/3} r^{2/3}, \tag{1.9b}$$

where $\langle \epsilon \rangle$ and $\langle \chi \rangle$ are respectively the average rate of dissipation of turbulent energy and temperature. The scaling laws (1.9) are called *Kolmogorov-Obukhov-Corrsin* scalings (K41-OC) and, as stated before, are expected for r sufficiently small. By considering a scale sufficiently small to make sure the homogeneous and isotropic hypothesis is still valid, but sufficiently large to make the buoyancy effect no more negligible, the following scaling laws can be obtained, called *Bolgiano-Obukhov* scalings (BO59)

$$\left\langle \delta u^2 \right\rangle (r) \sim \langle \chi \rangle^{2/5} (\alpha g)^{4/5} r^{6/5}, \tag{1.10a}$$

$$\left\langle \delta \theta^2 \right\rangle (r) \sim \langle \chi \rangle^{4/5} (\alpha g)^{-2/5} r^{2/5}. \tag{1.10b}$$

Here, αg is the additional parameter that describes the strength of buoyancy [8]. As stated before, when buoyancy is significant the BO59 scalings would hold, whereas when buoyancy is negligible, temperature behaves as a passive scalar and K41-OC scalings would hold. The buoyant term, estimated by $\alpha g \delta\theta(r) \delta u(r)$, increases with r; thus one expects a crossover from the K41-OC scalings to the BO59 scalings [8]. When comparing (1.9a) with (1.10a), or (1.9b) with (1.10b), it can be derived a cross-over scale between the two scalings, the so-called Bolgiano length L_B

$$L_B = \langle \epsilon \rangle^{5/4} \langle \chi \rangle^{-3/4} (\alpha g)^{-3/2}. \tag{1.11}$$

For $L_B \ll r \ll H$, one expects BO59 scalings, whereas for $\eta \ll r \ll L_B$ one expects K41-OC scalings, where η is the smallest length scale of turbulent motion, called Kolmogorov scale. This prediction, obtained by dimensional analysis,

is sketched in Figure 1.6. Despite the huge number of researches on the subject, evidences of the validity of the Bolgiano-Obuckhov scenario and the recovery of Kolmogorov-Obukhov-Corrsin scalings at small scale, as sketched in Figure 1.6, are still missing. There are many difficulties, both practical and as a matter of principle, in identifying this scenario, nevertheless future attempts will shed more light on this problem, allowing us a better understanding of turbulent dynamics for the modelling of Rayleigh-Bénard convection.

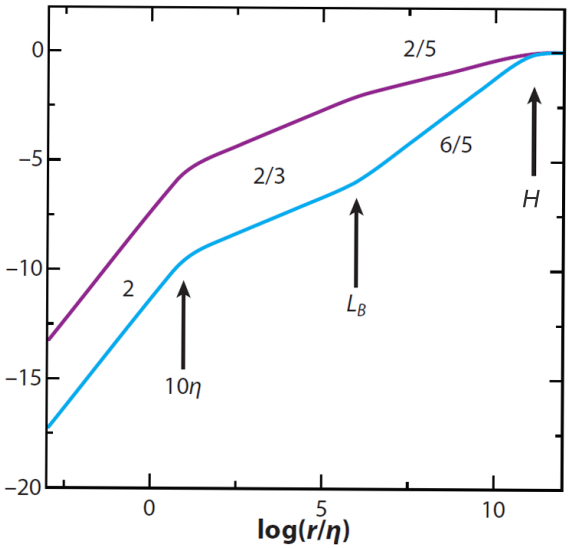

Figure 1.6: Sketch of the second-order velocity (blue curve) and temperature (purple curve), as they follow from dimensional analysis. This figure is adapted from [19], where more details can be found.

Chapter 2

Equations and numerical approach

2.1 The Oberbeck-Boussinesq equations

The Oberbeck-Boussinesq equations are widely used as a physical-mathematical model in the analysis of convection phenomena such as the Rayleigh-Bénard convection problem. The starting point for this model is to take the full set of compressible flow equations. By supposing that the gravitational force is the only body force present and that the fluid is a newtonian one with constant coefficient of viscosity μ, the equations of compressible flow can be rewritten as

$$\frac{D\rho}{Dt} + \rho\frac{\partial U_i}{\partial x_i} = 0, \tag{2.1a}$$

$$\rho\left(\frac{\partial U_i}{\partial t} + U_j\frac{\partial U_i}{\partial x_j}\right) = -\frac{\partial p}{\partial x_i} + 2\mu\frac{\partial S_{ij}}{\partial x_j} - \rho g\delta_{iz}, \tag{2.1b}$$

$$\rho T\frac{Ds}{Dt} = 2\mu S_{ij}S_{ij} - \frac{\partial q_i}{\partial x_i} + \rho Q, \tag{2.1c}$$

where i,j=x, y, z and δ_{ij} is the Kronecker delta. Here, $\rho(x, y, z, t)$, $U_i(x, y, z, t)$ and $p(x, y, z, t)$ are respectively the density, the velocity and the pressure fields. The tensor $S_{ij}(x, y, z, t)$, defined as

$$S_{ij} = \frac{1}{2}\left(\frac{\partial U_i}{\partial x_j} + \frac{\partial U_j}{\partial x_i}\right), \tag{2.2}$$

is the rate of strain. Quantity g is the gravitational acceleration, $T(x, y, z, t)$ is the temperature field, $s(x, y, z, t)$ is the entropy per unit mass, $q_i(x, y, z, t)$ is the rate of

heat flow per unit area and $Q(x, y, z, t)$ is the rate of internal heat generation per unit mass.

When there are variations in the temperature field T, the density of fluid changes. Anyway, when the temperature difference is small, the following approximation is feasible

$$\rho = \rho_0 + \delta\rho \approx \rho_0[1 - \alpha(T - T_0)], \tag{2.3}$$

where α is the coefficient of thermal expansion of the fluid, $T_0 = \langle T \rangle_{V,t}$ is the mean temperature of the system, ρ_0 is the density at T_0 and $\delta\rho$ is the change in density due to temperature variation. We use $\langle \cdot \rangle_V$ and $\langle \cdot \rangle_t$ to denote an average over the whole physical domain and an average over time, respectively. In the Oberbeck-Boussinesq approximation, $\delta\rho$ is taken to be small such that it is neglected in the continuity equation (2.1a), in the entropy equation (2.1c) and in the Navier-Stokes equations (2.1b) except in the buoyancy term $\rho g \delta_{iz}$ [8]. Hence, equations (2.1a) and (2.1b) can be rewritten as

$$\frac{\partial U_i}{\partial x_i} = 0, \tag{2.4a}$$

$$\rho_0 \left(\frac{\partial U_i}{\partial t} + U_j \frac{\partial U_i}{\partial x_j} \right) = -\frac{\partial p}{\partial x_i} + \mu \frac{\partial^2 U_i}{\partial x_j \partial x_j} - \rho_0 g \left[1 - \alpha \left(T - T_0 \right) \right] \delta_{iz}. \tag{2.4b}$$

As regards the entropy equation (2.1c), we assume $s(T, p)$ to be constant respect to the pressure, thus we have

$$ds = \left(\frac{\partial s}{\partial p} \right)_T dp + \left(\frac{\partial s}{\partial T} \right)_p dT = \left(\frac{\partial s}{\partial T} \right)_p dT. \tag{2.5}$$

By recalling the state equation for the enthalpy and by supposing negligible the differential of the pressure, we obtain

$$dh = Tds + \frac{dp}{\rho} \approx Tds. \tag{2.6}$$

Finally, the exact differential of the entropy can be written as

$$ds = \left(\frac{\partial h}{\partial T} \right)_p \frac{dT}{T} = c_p \frac{dT}{T}, \tag{2.7}$$

where c_p is the specific heat at constant pressure. We take $2\mu S_{ij}S_{ij}$, which is the rate of internal heat generation per unit mass due to the mechanical dissipation, and Q to be small such that they are neglected, hence we can recast the entropy equation into

$$\rho c_p \frac{DT}{Dt} = k \frac{\partial^2 T}{\partial x_i \partial x_i}, \tag{2.8}$$

which is the equation for the temperature. Here, k is the thermal conductivity.

We group together equation (2.4a), (2.4b) and (2.8), then, by introducing some auxiliary variables, we obtain the set of the Oberbeck-Boussinesq equations

$$\frac{\partial U_i}{\partial x_i} = 0, \tag{2.9a}$$

$$\frac{\partial U_i}{\partial t} + U_j \frac{\partial U_i}{\partial x_j} = -\frac{1}{\rho_0}\frac{\partial p^*}{\partial x_i} + \nu \frac{\partial^2 U_i}{\partial x_j \partial x_j} + \alpha g \Theta \delta_{iz}, \tag{2.9b}$$

$$\frac{\partial \Theta}{\partial t} + U_j \frac{\partial \Theta}{\partial x_j} = \kappa \frac{\partial^2 \Theta}{\partial x_i \partial x_i}. \tag{2.9c}$$

Here, $p^*(x, y, z, t) = p(x, y, z, t) + \rho_0 \Psi(x, y, z, t)$ is the modified pressure, where Ψ is the gravitational potential. Quantity $\nu = \mu/\rho$ is the kinematic viscosity, $\kappa = k/(c_p \rho)$ is thermal diffusivity and finally the variable $\Theta(x, y, z, t) = T(x, y, z, t) - T_0$ is the temperature deviation from the mean. The Oberbeck-Boussinesq equations are one vector and two scalar equations for the one vector and two scalar variables U_i, p^* and Θ. It is useful to have names for some terms. The last term on the right-hand side of (2.9b), $\alpha g \Theta \delta_{iz}$, is known as the buoyancy force (even when Θ is negative and the term represents the tendency for heavy fluid to sink). The term on the right-hand side of (2.9c) is the conduction term, which represents the conductive transport of heat [29].

The range of validity of the Oberbeck-Boussinesq approximation is usually estimated by [6]

$$\alpha \Delta T < 0.1 \div 0.2, \tag{2.10}$$

Furthermore, the height of the physical domain, H, must be small enough so that the hydrostatic pressure gradient along the direction of gravity acceleration is negligible.

Using H as a characteristic length scale, H/U_f as a characteristic time scale

and ΔT as characteristic temperature scale, where $U_f = \sqrt{g\alpha\Delta T H}$ is the free-fall velocity, we can rewrite the equations (2.9) in a dimensionless form

$$\frac{\partial U_i}{\partial x_i} = 0, \tag{2.11a}$$

$$\frac{\partial U_i}{\partial t} + U_j \frac{\partial U_i}{\partial x_j} = -\frac{\partial p^*}{\partial x_i} + \sqrt{\frac{Pr}{Ra}} \frac{\partial^2 U_i}{\partial x_j \partial x_j} + \Theta \delta_{iz}, \tag{2.11b}$$

$$\frac{\partial \Theta}{\partial t} + U_j \frac{\partial \Theta}{\partial x_j} = \frac{1}{\sqrt{PrRa}} \frac{\partial^2 \Theta}{\partial x_i \partial x_i}. \tag{2.11c}$$

We use the same symbols for the dimensionless quantities to streamline the notations. In the following dissertation, only dimensionless quantities are used. The dimensional ones, when used, are explicitly specified.

To complete the model, we need to specify the spatial domain and the boundary conditions for U_i and Θ. We select a rectangular cell as the spatial domain (see Figure 1.2(a)). The Cartesian coordinate system is cell-centered, with the xy-plane parallel to the horizontal plates and the z-axis pointing in the direction opposite to that of gravity acceleration. Periodic boundary conditions are imposed in the horizontal directions x and y, in order to maintain homogeneity and isotropy on horizontal planes. Isothermal and no-slip boundary conditions are used on the top/bottom plates for the temperature and velocity fields respectively

$$\Theta\left(x, y, z = -1/2, t\right) = -\Theta\left(x, y, z = 1/2, t\right) = 1/2 \tag{2.12a}$$

$$U_i\left(x, y, z = -1/2, t\right) = U_i\left(x, y, z = 1/2, t\right) = 0. \tag{2.12b}$$

Using the temperature equations and the boundary conditions just defined, a new expression for the Nusselt number, previously introduced in (1.3), can be obtained. First we take the horizontal plane average, $\langle\cdot\rangle_A$, of the dimensional temperature equation (2.9c)

$$\frac{\partial \langle\Theta\rangle_A}{\partial t} + \frac{\partial \langle W\Theta\rangle_A}{\partial z} = \kappa \frac{\partial^2 \langle\Theta\rangle_A}{\partial z^2}, \tag{2.13}$$

where $U_z = W$. The relation $\partial \langle U_j\Theta\rangle_A / \partial x_j = U_j \partial \langle\Theta\rangle_A / \partial x_j$ ensues from the equation of continuity (2.9a). Supposing steady-state flow i.e. $\partial <>_A / \partial t = 0$, we

integrate equation (2.13) from $z = -H/2$ to a generic z

$$\langle W\Theta \rangle_A - \langle W\Theta \rangle_A |_{z=-H/2} = \kappa \frac{d \langle \Theta \rangle_A}{dz} - \kappa \frac{d \langle \Theta \rangle_A}{dz}\bigg|_{z=-H/2}. \tag{2.14}$$

where $\langle W\Theta \rangle_A$ and $-\kappa(d \langle \Theta \rangle_A / dz)$ are respectively the convective and the conductive contributions to the heat flux across the horizontal plane at height z. Accounting for the no-slip boundary conditions, it follows that $\langle W\Theta \rangle_A |_{z=-H/2} = 0$. Since the heat flux through the horizontal walls ϕ is equal to $-\kappa(d\langle \Theta \rangle_A / dz)|_{z=-H/2}$, the Nusselt number can be rewritten as

$$Nu = -\frac{H}{\Delta T} \frac{d \langle \Theta \rangle_A}{dz}\bigg|_{z=-H/2} = H \frac{\langle W\Theta \rangle_A - \kappa \frac{d\langle \Theta \rangle_A}{dz}}{\kappa \Delta T}. \tag{2.15}$$

Hence, the conductive heat flux at the walls, which defines the Nusselt number, is controlled by the convective contributions to the heat flux away from the walls, highlighting how the core flow influences the near-wall heat exchange.

2.2 Simulation details

The Oberbeck-Boussinesq equations describe all features of the turbulent Rayleigh-Bernard convection, from the largest to the smallest length and time scales. However, analytical solutions do not exist even for the simplest turbulent flows and numerical solutions are required.

The explosive growth of computational power in the last three decades, has generated huge interest in the area of numerical simulation of turbulence. Computational studies have also gained momentum with the advent of efficient and accurate numerical schemes for solving coupled and highly nonlinear partial differential equations that are used to describe turbulent flows.

Simulation methodologies can again be classified, based on the level of representation of the physics and accuracy, into Reynolds-Averaged Navier-Stokes (RANS), Large-Eddy Simulation (LES) and Direct Numerical Simulation (DNS) approaches [25]. The RANS approach involves the solution of the Reynolds equations to determine the mean fields. The Reynolds stresses, which appear as unknowns in the Reynolds equations, are determined by a turbulence model, named Reynolds-stress model. In LES, the larger turbulent motions are directly resolved, whereas the ef-

fects of the smaller-scale motions are modelled [22]. Direct numerical simulations discretize the governing equations on a spatio-temporal grid and solve them with initial and boundary conditions appropriate to the flow considered. Unlike RANS and LES, no model for turbulent fluctuations is used, hence the fundamental requirement for conducting DNS is to resolve all the smallest scales of turbulence i.e. the *Kolmogorov scales* or the *Batchelor scales*.

The characteristic scales of the smallest turbulent *motion* are the Kolmogorov length (η), time (τ_η) and velocity (u_η) scales, formed from the mean dissipation rate $\langle\epsilon\rangle$ and the kinematic viscosity ν as follows

$$\eta = \left(\frac{\nu^3}{\langle\epsilon\rangle}\right)^{1/4}, \qquad \tau_\eta = \left(\frac{\nu}{\langle\epsilon\rangle}\right)^{1/2}, \qquad u_\eta = \left(\nu\langle\epsilon\rangle\right)^{1/4}. \tag{2.16}$$

On the other hand, Bachelor scales characterize the very smallest structures of a turbulent *scalar field*, which is the temperature one in this case. Similarly, the Bachelor length (λ), time (τ_λ) and velocity (u_λ) scales are defined by using $\langle\epsilon\rangle$ and κ, thus they can be written as

$$\lambda = \left(\frac{\kappa^3}{\langle\epsilon\rangle}\right)^{1/4}, \qquad \tau_\lambda = \left(\frac{\kappa}{\langle\epsilon\rangle}\right)^{1/2}, \qquad u_\lambda = \left(\kappa\langle\epsilon\rangle\right)^{1/4}. \tag{2.17}$$

By recalling the definition of the Prandtl number, the ratio of the Kolmogorov scales to the equivalent Bachelor scales can be written as

$$\frac{\eta}{\lambda} = Pr^{3/4}, \qquad \frac{\tau_\eta}{\tau_\lambda} = Pr^{1/2} \qquad \frac{u_\eta}{u_\lambda} = Pr^{1/4}, \tag{2.18}$$

hence, for $Pr < 1$ the Kolmogorov scales are the smallest ones to be resolved by the DNS whereas, for $Pr > 1$, the resolution requirement is given by the Bachelor scales. Using an exact relation for $\langle\epsilon\rangle$ (see Appendix A), we can rewrite η and λ as

$$\eta = H\left(\frac{Pr^2}{RaNu}\right)^{1/4}, \qquad \lambda = H\left(\frac{1}{RaPrNu}\right). \tag{2.19}$$

Similar relations can be obtained for the time and velocity scales. Since Nu is an output parameter, the smallest scales of motion are unknown a priori. Nevertheless, many simulation in literature provide verified resolutions which possibly represent a good starting point for a trial-and-error approach.

The direct numerical simulations presented in this thesis are performed using a spectral method which discretizes space with N_z Chebychev polynomials in the z direction and with N_x and N_y Fourier modes in the x and y directions respectively. Time integration is performed with a fourth order Runge-Kutta scheme for the non-linear terms and a second order accurate Crank-Nicholson scheme for the linear ones.

Specifically, the numerical method resolves the velocity-vorticity formulation of the Oberbeck-Boussinesq equations. This formulation is an alternative form of the governing equation, which does not include pressure [23]. The unknown field functions are the the normal velocity W, the normal vorticity ω and the temperature Θ. Once the the normal velocity and the normal vorticity have been calculated, the other velocity components can be found form the incompressibility constraint and the definition of the normal vorticity. The vorticity-velocity methods present some advantages compared with the classical formulation on primitive variables or with the vorticity-stream function methods. The main advantage is that the resulting algorithm for the resolution of the Oberbeck-Boussinesq equations is quite simple compared with the other formulations. Moreover, the physic of the problem does not change from a formulation to another one, therefore the strong point of the vorticity-velocity methods is only numerical.

Finite difference methods for the direct numerical solution of the governing equations, like finite element methods, are based on *local representations* of functions, usually by low order polynomials. In contrast spectral methods make use of *global representations* usually by high-order polynomials, such as Chebychev polynomials, or Fourier series. Under many circumstances the result is a degree of accuracy that local methods cannot match. For large-scale computations, especially in three-dimensional space domains, this higher accuracy may be decisive to allow a coarser mesh, hence a smaller number of data values to store and operate upon [28].

At any given instant in time, the spectral representation of the numerical solution consists of $N_x \times N_y \times N_z$ wavenumbers for both the velocity U_i and the temperature Θ fields. This spectral representation is equivalent to representing U_i and Θ in the physical space on a $N_x \times N_y \times N_z$ grid. Along the x and y directions there are nodes with uniform spacings $\Delta x = L_x/N_x$ and $\Delta y = L_y/N_y$, where the rectangular box with dimensions $L_x \times L_y \times H$ is the solution domain. In the z direction, the grid spacing is non-uniform with, conveniently, a finer grid spacing near the boundaries.

Anyway, we define $\Delta z = L_z/N_z$ as the average grid width along z.

The maximum wavenumber i.e. the maximum frequency of turbulent eddies which the grid is capable to resolve, is $k_{max} = \pi/h$, where $h = max(\Delta x, \Delta y, \Delta z)$ is the maximum grid width. Moreover, to fulfill the resolution requirement, the wavenumber k_{max} must be greater than π/η for $Pr \leq 1$, and greater than π/λ for $Pr \geq 1$. All the simulations are conducted in a rectangular cell of aspect-ratio $\Gamma = 8$ i.e. $L_x = L_y = 8 \cdot H$ (see Figure 2.1). By discretizing all directions with the same number of spectral modes, then $\Delta x = L_x/N_x = L_y/N_y$ and $\Delta x > \Delta z$. For this reason, the maximum grid width h is equal to Δx or Δy and the upper bounds to the grid width can be written as

$$\frac{1}{\pi}\frac{\Delta x}{\eta} \leq 1, \;\; Pr \leq 1; \qquad \frac{1}{\pi}\frac{\Delta x}{\lambda} \leq 1, \;\; Pr \geq 1. \tag{2.20a}$$

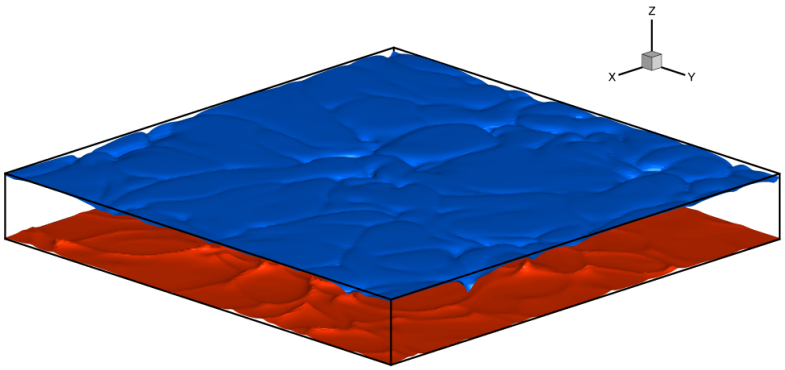

Figure 2.1: The Rayleigh-Bénard convection setup selected for the DNS. Two iso-surface of temperature are visualized: hot at the bottom ($\Theta = 0.4$) in red, cold at the top ($\Theta = -0.4$) in blue. DNS result for $Ra = 1.7 \cdot 10^5$ and $Pr = 0.7$.

Concerning the temporal resolution, it is necessary that a fluid particle move only a fraction of the maximum grid spacing h in a time step Δt. As a consequence, the time step employed must satisfy the CFL-condition (Courant-Levy-Friedrichs), otherwise the simulation will produce incorrect results. In practice, the CFL-condition imposed is found to be approximately [22]

$$C = \frac{\langle k \rangle^{1/2} \Delta t}{h} = \frac{1}{20} \tag{2.21}$$

where C is the Courant number and $\langle k \rangle$ is the turbulent kinetic energy.

In order to accumulate reliable statistics, velocity and temperature fields are

saved after the initial transient has suppressed and with a time step large enough to guarantee temporally uncorrelated configurations. Let t^* be the characteristic time of the large-scale circulation, defined as

$$t^* = 2\frac{H}{\sqrt{g\alpha\Delta T H}}, \tag{2.22}$$

and let Δt_s be the time interval between two storages, then $\Delta t_s/t^* > 1$ is a necessary and sufficient condition to obtain temporally uncorrelated fields.

The parameters and resolution settings of the simulations are given in Table 2.1. DNS are performed at the same Ra and at different Pr to investigate the effects of the last parameter on the flow. With the available computational resources, only low Ra flows were reachable. Indeed, the resolution requirements increase with Ra and so does the computational load, as can be seen from the relations (2.19).

It should be noted that a $128\times128\times129$ grid is suitable for all the simulations (as stated previously, a posteriori validation is applied to the resolution). The time step is not reported because it is adaptive, which means that it is periodically updated to fulfill the minimum CFL condition. Finally, the time interval between two successive storages fully satisfies the requirement.

Ra	Pr	Re	$\Delta t_s/t^*$	$\Delta x/\pi\eta_K$	$\Delta x/\pi\eta_T$	$N_x \times N_y \times N_z$
1.7×10^5	0.7	493	10	0.72	0.56	$128 \times 128 \times 129$
1.7×10^5	2.0	292	10	0.43	0.73	$128 \times 128 \times 129$
2.1×10^5	7.0	172	10	0.25	1.05	$128 \times 128 \times 129$

Table 2.1: Simulation parameters.

Chapter 3

Numerical results

3.1 Instantaneous fields

In order to identify specific flow regions and characteristic structures, a preliminary approach to the study of turbulent Rayleigh-Bénard convection consists of analyzing the temperature and velocity fields obtained by DNS. Figures 3.1, 3.2 and 3.3 show instantaneous velocity field (arrows) superimposed on the instantaneous surface temperature field (colored area) for different Pr. As can be seen in the vertical slices xz plotted in Figure 3.1(c), 3.2(c) and 3.3(c), a recurrent coherent structure is present, consisting of a localized portion of fluid having a temperature contrast with the background. This structure, named *thermal plume*, plays a fundamental role in turbulent convection as it carries a large fraction of the heat into the core of the flow.

Hot and cold plumes detach respectively from the bottom and the upper plate, moving toward the core of the cell driven by buoyancy forces, which are triggered by a density contrast with the ambient. As heated fluid rises, it pushes aside the cooler fluid above it. As can be clearly seen in the vertical slices, the rising fluid produces a stalk, while the deflected fluid produces a cap on top. As the pushing and deflection continue, the edge of the cap may further fold over, creating a mushroom-like structure [15]. The same behaviour affects cooled descending plumes.

Many studies [16][26][31] have shown two different morphologies for the plume: the *sheet-like plume*, which is observable close to the walls, and the *mushroom-like plume*, which is observable in the core. Figure 3.1(a), 3.2(a) and 3.3(a) show a horizontal xy slice of an instantaneous temperature field close to the wall for each

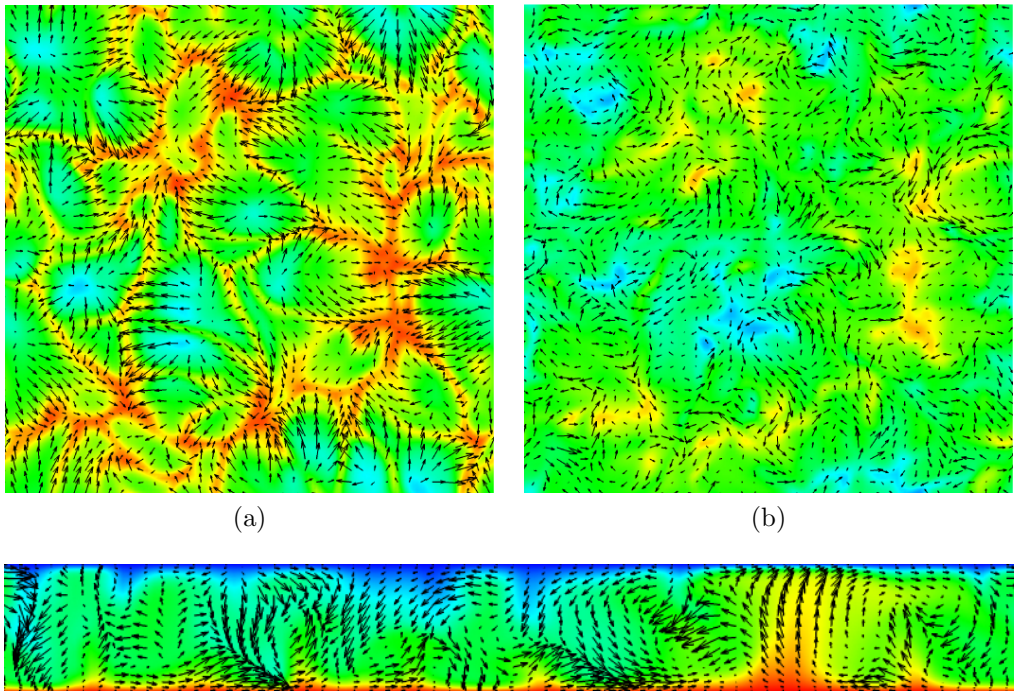

(a) (b)

(c)

Figure 3.1: Cross-sections of the temperature Θ with superimposed velocity vectors for the $Pr = 0.7$ DNS. The slices shown are (a) a horizontal slice at the edge of the thermal boundary layer, (b) a horizontal slice through the centre, (c) a vertical slice through the centre. The colour scales range from blue (negative values) through green (zero) to red (positive values).

Prandtl number considered. A fine network of thin plumes is visible. The sheet-like structures are formed by impingement of cold plumes onto the bottom plate, as the hot fluid in the boundary layer is pushed away. As expected, sheet-like plumes become thinner as the Prandtl number increases due to the smaller thermal diffusivity, in comparison with the kinematic viscosity.

The horizontal xy slices through the centre of the cell are plotted in Figure 3.1(b), 3.2(b) and 3.3(b). The pattern of sheet-like plumes is almost lost in the middle cross-section and horizontal vortical structures are visible. Therefore, the slices through the centre of the cell likely to be horizontal cuts of mushroom-like plumes. By comparing the middle cross-sections at different Pr, we observe larger mushroom-like plume sections at higher Pr. It seems like sheet-like plumes, which are very thin due to high Pr, cluster together creating a set of massive mushroom-like structures.

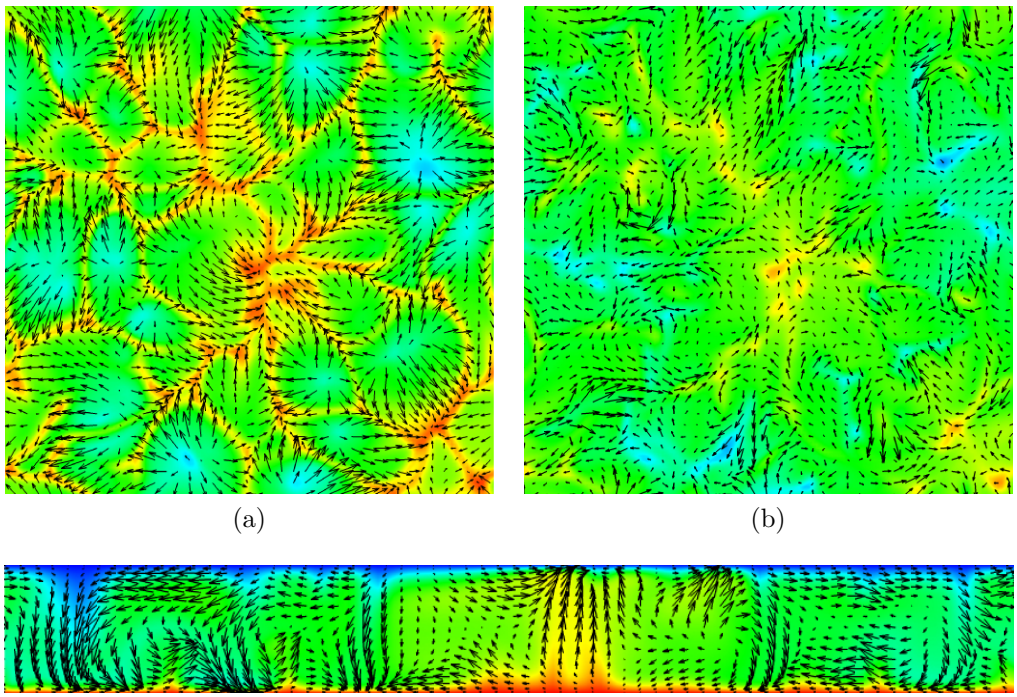

(a) (b)

(c)

Figure 3.2: Cross-sections, as in Figure 3.1, of the temperature Θ for the $Pr = 2$ DNS.

The transition from sheet-like plumes to mushroom-like ones is clearly shown in the vertical xz slices. The tendency of the plume to broaden with distance from its source, getting swept and tilted, is a statement of its tendency to become turbulent and entrain ambient fluid. As the laminar, sheet-like plumes move away from the walls, a free shear layer will develop at its boundaries with the ambient fluid. This shear layer will be subjected to the same type of shear flows instabilities experienced by mixing layers and as a result it will "roll up" under the influence of coherent structures or large eddies [21], represented in Figure 3.4 by red surfaces (see Appendix B for further details about the plotted quantity). As in the free shear layers, these eddies initiate the transition to fully developed turbulent flow, in this case a turbulent, mushroom-like plume.

Hot and cold plumes do not collide, but group together to create a set of circulating cells, having a characteristic length comparable with the height of the cell. The formation of these structures of the velocity field, named large-scale circulations, is inevitable due to the positive feedback resulting from the interaction between the

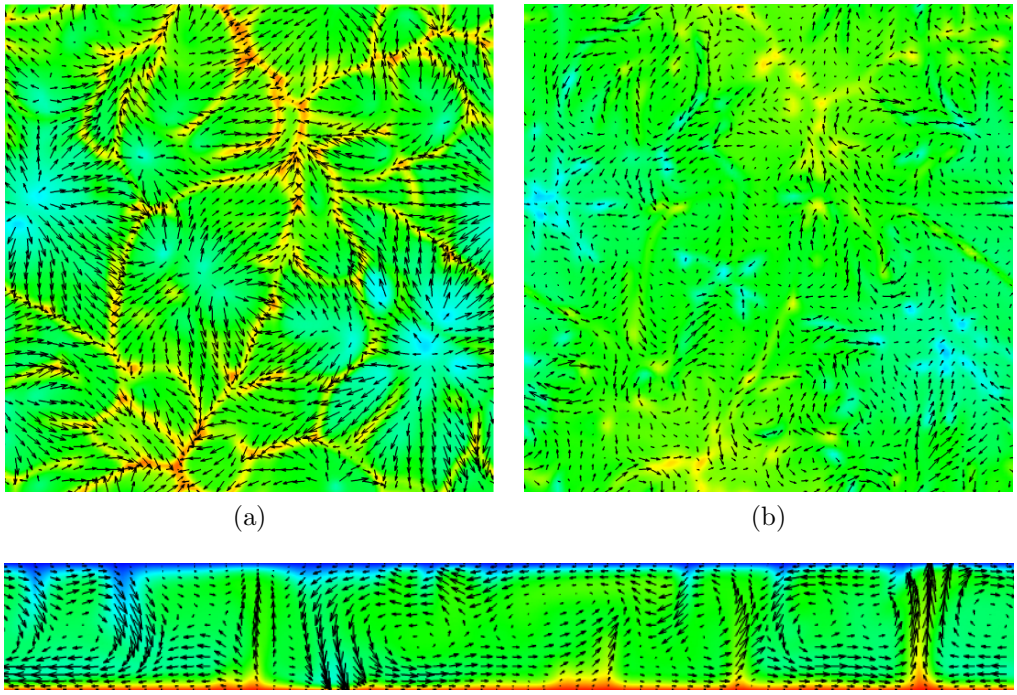

(a) (b)

(c)

Figure 3.3: Cross-sections, as in Figure 3.1, of the temperature Θ for the $Pr = 7$ DNS.

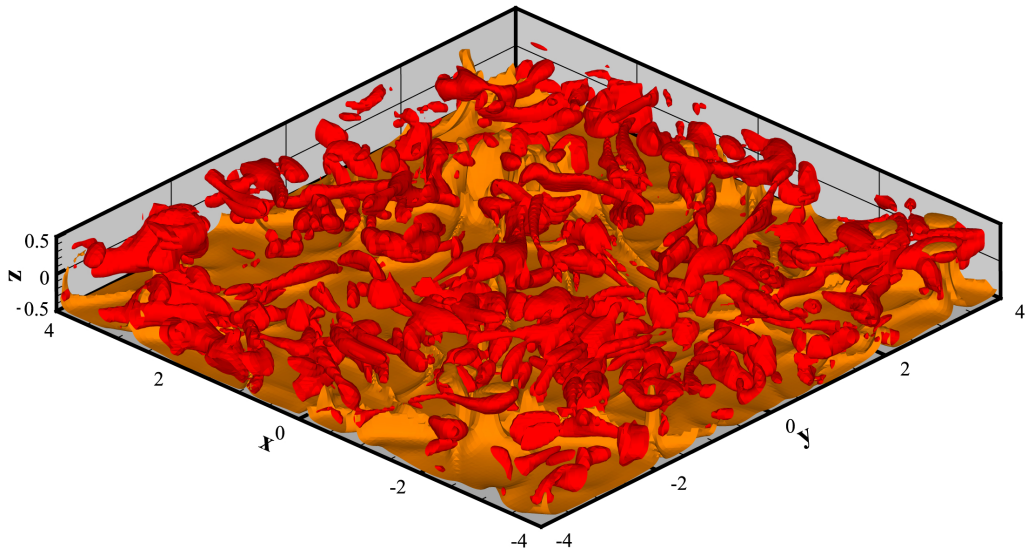

Figure 3.4: Snapshot of turbulent Rayleigh-Bénard convection at $Pr = 7$. Plumes are clearly visible through the orange isosurface of temperature ($\Theta = 0.2$), whereas the red surfaces reveal the vortical structures.

temperature field and the circulation itself. Qualitatively, the plumes impingement generates horizontal pressure gradients at the top and bottom walls that drive a mean flow which transports a relatively large amount of thermal energy through the bottom layers. The net transport of thermal energy toward the region with ascending flow causes spatial temperature gradients. Finally, these spatial temperature differences induce spatial gradients in the buoyancy which completes the feedback loop [30].

3.2 Mean and root mean square

A first statistical approach to the study of turbulent Rayleigh-Bénard convection is the analysis of one-point statistics. The simplest statistical properties are the mean, or first moment, and the variance, or second moment, which allow a rough characterization of the flow. We start by introducing the decomposition of the velocity $U_i(x, y, z, t)$ and the temperature $\Theta(x, y, z, t)$ fields into mean, $\langle U_i(x, y, z, t)\rangle$ and $\langle\Theta(x, y, z, t)\rangle$ respectively, and fluctuation

$$u_i(x, y, z, t) = U(x, y, z, t) - \langle U_i(x, y, z, t)\rangle\,, \tag{3.1}$$

$$\theta(x, y, z, t) = \Theta(x, y, z, t) - \langle\Theta(x, y, z, t)\rangle\,. \tag{3.2}$$

This decomposition is referred to as the *Reynolds decomposition*, i.e. [22]

$$U_i(x, y, z, t) = u_i(x, y, z, t) + \langle U_i(x, y, z, t)\rangle \tag{3.3}$$

$$\Theta(x, y, z, t) = \theta(x, y, z, t) + \langle\Theta(x, y, z, t)\rangle\,. \tag{3.4}$$

Thermal gradients are the driving factor of Rayleigh-Bénard convection, therefore a good starting point for providing a topological characterization of the flow is to analyze one-point statistics of the temperature field. Figure 3.5(a) plots the mean temperature as a function of z and for different Prandtl numbers. Two well separated regions are clearly observable: a gradient-dominated layer next to the horizontal plates and a nearly isothermal region in the center.

By recalling the Nusselt number defined in (2.15), we can state that the heat transport is mostly conductive close to the walls and is mostly convective in the central region. The conductive layer, made of quiescent fluid, it is called *thermal boundary layer*. On the other hand, the central, nearly isothermal region, is called

bulk. Now we focus on the thermal boundary layer; this region is defined in terms of its thickness δ_t as

$$\delta_t = \frac{H}{2Nu} = -\frac{\Delta T}{2}\frac{d\langle\Theta\rangle}{dz}\bigg|_{z=-H/2}, \tag{3.5}$$

which is the distance from the horizontal walls supporting a temperature difference roughly equal to $\Delta T/2$. The peak distance of the root mean square (r.m.s.) temperature $\sqrt{\langle\theta^2\rangle}$ from the plates is another definition of the thermal boundary layer thickness, hereafter referred to as δ_t^{rms}.

By measuring $d\langle\Theta\rangle/dz$ at the walls, we can obtain the Nusselt number for all the DNS. As can be seen in Table 3.1, Nu increases with Pr and, therefore, δ_t

	Pr=0.7	Pr=2	Pr=7
Nu	5.0	5.1	5.2

Table 3.1: Nusselt numbers at different Pr

decreases by definition. Anyway, the variation in thickness is so small that in Figure 3.5(a) only an average value of δ_t is plotted. A comparison between Figure 3.5(a) and (b) clearly indicates that both methods for extracting the thermal boundary layer lead to the same result, which means that the average δ_t^{rms} is nearly equal to the average δ_t. We have separated the thermal boundary layer from the rest of the flow by defining its thickness, nevertheless it is still not clear what mechanism regulates the characteristic dimension of this layer. To that end, we introduce a local Rayleigh number

$$Ra_\delta = \frac{g\alpha\Delta T\delta_t^3}{\nu\kappa}, \tag{3.6}$$

where δ_t is the characteristic length. The thickness δ_t is regulated by the local Rayleigh number in the sense that Ra_δ must be approximately equal to the critical Rayleigh number Ra_c, as a sign of the thermal boundary layer marginal stability. Indeed, when Ra_δ exceeds Ra_c in a specific location, the boundary layer detaches permanently from there, as the buoyancy forces prevail on dampening effects, and a thickness is restored so that $Ra_\delta \approx Ra_c$.

The presence of large-scale structures of the velocity field, which develop both

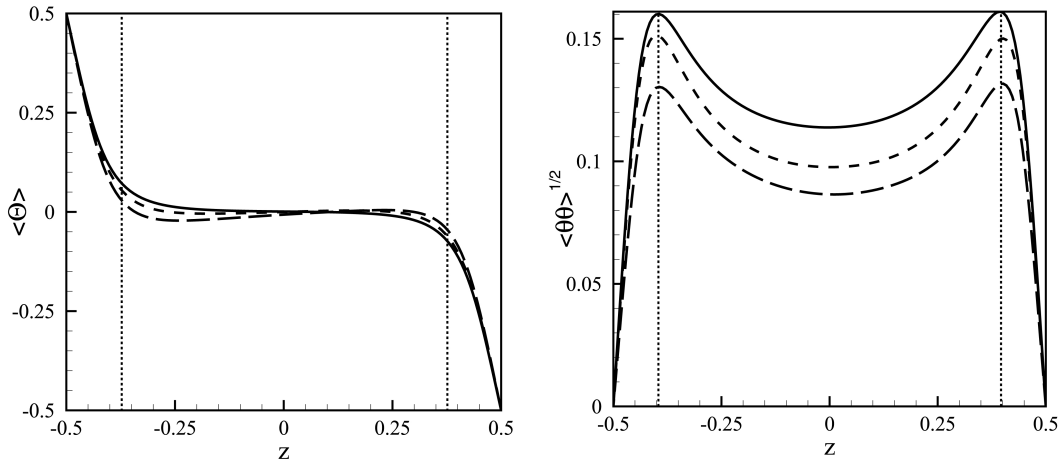

Figure 3.5: (a) The mean temperature $\langle\Theta\rangle$ and (b) the r.m.s. temperature $\sqrt{\langle\theta^2\rangle}$ as a function of z, for $Pr = 0.7$ (solid line), $Pr = 2$ (dashed line) and $Pr = 7$ (long dashed line). The average of δ_t/H and δ_t^{rms}/H over the three simulations are plotted respectively in (a) and (b) with dotted lines.

for confined and unconfined domains i.e. periodic boundary conditions on sidewalls [30], generate two viscous boundary layer just below the top and just above the bottom plate. The viscous boundary layer thickness δ_ν is commonly defined as the peak position of $\sqrt{\langle u^2\rangle}$ or $\sqrt{\langle v^2\rangle}$, the r.m.s. horizontal velocities. As can be seen in Figure 3.6(a), δ_ν shows clear dependence on the Prandtl number and in particular δ_ν increases with Pr. Since the thermal boundary layer thickness is almost constant, the ratio δ_ν to δ_t also increases with Pr. This result agrees with the Grossmann-Lohse theory [13], in which a viscous, Blasius-type boundary layer is assumed, with a thickness

$$\delta_\nu \sim \frac{H}{\sqrt{Re}}, \tag{3.7}$$

where the characteristic velocity of the Reynolds number is the r.m.s. horizontal velocity, probing the large-scale turbulence and thus the large-scale circulations. By recalling equation (3.5), we obtain the ratio of δ_ν to δ_t predicted by the Grossmann-Lohse theory

$$\frac{\delta_\nu}{\delta_t} \sim \frac{Nu}{2\sqrt{Re}}. \tag{3.8}$$

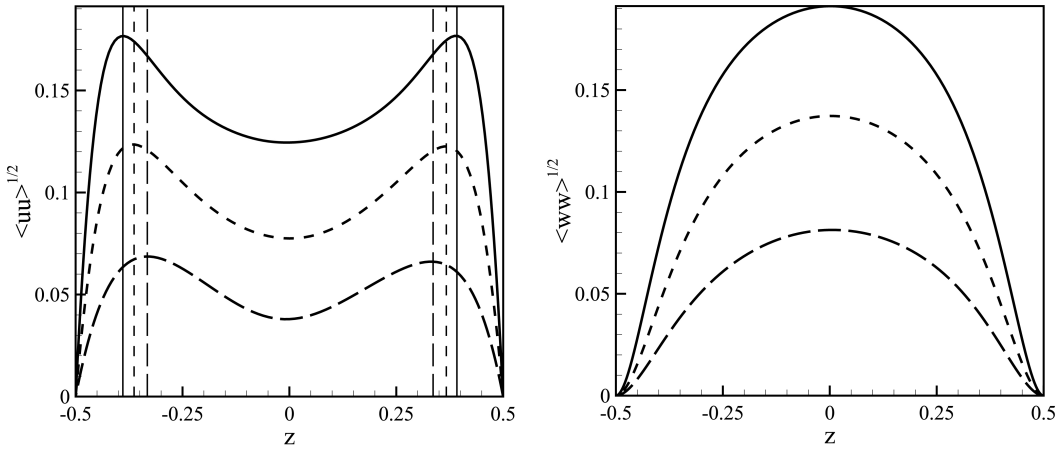

Figure 3.6: (a) The r.m.s. velocity $\sqrt{\langle u^2 \rangle}$ and (b) the r.m.s. velocity $\sqrt{\langle w^2 \rangle}$ as a function of z, for $Pr = 0.7$ (solid line), $Pr = 2$ (dashed line) and $Pr = 7$ (long dashed line). The viscous boundary layer thickness δ_ν / H is shown in (a) for the three simulations.

Furthermore, it becomes clear from Table 3.1 and Figure 3.6 that at higher Pr the Nu is almost constant whereas Re is smaller, as the r.m.s. horizontal velocity is smaller. Consequently, the theoretically-based ratio (3.8) increases with the Prandtl number according to the DNS single-point statistics. This result confirms the presence of laminar boundary layers next to the walls, as can be expected from the low Rayleigh number at which DNS are conducted.

The characteristic size of the bulk is much greater than δ_t or δ_ν, and it is comparable with the height of the cell H. Along this zone, fragments of the thermal boundary layers are transported by buoyancy forces, which are accompanied by a broadening of these structures due to diffusion and mixing by turbulent fluid [6]. Since the temperature derivative is almost zero, the heat flux across the bulk is mainly convective and it originates from the interaction of the mean temperature field and the vertical velocity fluctuations, measured by $\sqrt{\langle w^2 \rangle}$ and plotted in Figure 3.6b.

As can be seen from these single-point statistics, turbulent Rayleigh-Bénard convection is thermodynamically a heat engine, made of different working parts [29]. Heat enters the fluid at hot boundaries, is transported through the bulk mainly by convection, and leaves it at colder boundaries. Inside the flow, the thermal energy is converted into kinetic energy by buoyancy forces, then it is distributed

and dissipated within the fluid. To display all these mechanisms, the analysis of the turbulent kinetic energy budget is performed in the next section.

3.3 Turbulent kinetic energy equation

The evaluation of the turbulent kinetic energy budget is mandatory to obtain a clearer picture of the turbulent convection, therefore a detailed examination of one-point statistics such production, dissipation and spatial redistribution of turbulent kinetic energy is carried on. The intensity of turbulence at a certain point in the geometric domain is related to the so-called instantaneous turbulent kinetic energy density, defined as

$$k = \frac{1}{2} u_i u_i \tag{3.9}$$

Using the Oberbek-Boussinesq equations (2.11), one can derive an evolution equation for k. By subtracting the average of (2.11) from (2.11), we obtain a set of equations for the fluctuations. Horizontal isotropy and homogeneity, together with the no-slip condition at the top and bottom plates, yield $\langle U_i \rangle = 0$. Therefore the equations for the fluctuations can be written as

$$\frac{\partial u_i}{\partial x_i} = 0, \tag{3.10a}$$

$$\frac{\partial u_i}{\partial t} + u_j \frac{\partial u_i}{\partial x_j} = \frac{\partial \langle u_i u_j \rangle}{\partial x_j} - \frac{\partial p^{'}}{\partial x_i} + \sqrt{\frac{Pr}{Ra}} \frac{\partial^2 u_i}{\partial x_j \partial x_j} + \theta \delta_{iz}, \tag{3.10b}$$

$$\frac{\partial \theta}{\partial t} + \frac{\partial \langle u_j \theta \rangle}{\partial x_j} = \frac{1}{\sqrt{PrRa}} \frac{\partial^2 \theta}{\partial x_j \partial x_j}, \tag{3.10c}$$

where $p^{'} = p^* - \langle p^* \rangle$ is the pressure fluctuation. Taking the scalar product of equation (3.10b) with u_i and then taking the ensemble average, yield

$$\frac{\partial \langle k \rangle}{\partial t} + \frac{\partial \langle k u_j \rangle}{\partial x_j} = -\frac{\partial \left\langle u_i p^{'} \right\rangle}{\partial x_i} + \sqrt{\frac{Pr}{Ra}} \left\langle u_i \frac{\partial^2 u_i}{\partial x_j \partial x_j} \right\rangle + \langle u_i \theta \rangle \, \delta_{iz} \tag{3.11}$$

When the flow is in the stationary state, $\partial <> / \partial t$ vanishes. After some manipulation, we get

$$- \frac{\partial \langle k u_j \rangle}{\partial x_j} - \frac{\partial \left\langle u_i p^{'} \right\rangle}{\partial x_i} + \sqrt{\frac{Pr}{Ra}} \frac{\partial^2 \langle k \rangle}{\partial x_j \partial x_j} + \langle w \theta \rangle - \langle \tilde{\epsilon} \rangle = 0. \tag{3.12}$$

Here, $w = W - \langle W \rangle$ is the vertical velocity component fluctuation and $\langle \tilde{\epsilon} \rangle$ is the average rate of pseudo-dissipation, defined as

$$\langle \tilde{\epsilon} \rangle = \sqrt{\frac{Pr}{Ra}} \left\langle \frac{\partial u_i}{\partial x_j} \frac{\partial u_i}{\partial x_j} \right\rangle = \langle \epsilon \rangle - \sqrt{\frac{Pr}{Ra}} \frac{\partial^2 \langle u_i u_j \rangle}{\partial x_i \partial x_j}, \tag{3.13}$$

where $\langle \epsilon \rangle$ is the average rate of "real" dissipation. In virtually all circumstances the final term in (3.13) is small and consequently the distinction between $\langle \epsilon \rangle$ and $\langle \tilde{\epsilon} \rangle$ is seldom important [22]. Because of the horizontal isotropy and homogeneity, $\partial <> /\partial x = \partial <> /\partial y = 0$, hence we can rewrite (3.12) as

$$-\frac{d \langle kw \rangle}{dz} - \frac{d \langle wp' \rangle}{dz} + \sqrt{\frac{Pr}{Ra}} \frac{d^2 \langle k \rangle}{dz^2} + \langle w\theta \rangle - \langle \tilde{\epsilon} \rangle = 0, \tag{3.14}$$

which is the so-called turbulent kinetic energy equation. The first three terms are, respectively, the inertial, the pressure-velocity and the viscous contribution to the turbulent kinetic energy transport (per unit mass) across the horizontal planes of the cell. The last two terms are, respectively, a source and a sink of energy in the k equation and are called production and dissipation.

The different terms in the turbulent kinetic energy equation (3.14), are reported in Figure 3.7 for the $Pr = 0.7$ simulation. Two distinct regions are clearly recognizable in the flow: a core homogeneous region in which the terms are almost constant, and a inhomogeneous layer close to the wall. By inspecting Figure 3.6(a), it is possible to identify the homogeneous and the inhomogeneous layer with the bulk and the viscous boundary layer respectively.

The production term is dominant in the bulk, where it exceeds dissipation by a factor of around 1.8. The excess energy produced is carried away by the transport terms and sent toward the wall, where energy dissipation dominates. The negative value of the transport indicates the extraction and the positive values indicates the supply of energy to the corresponding region. Figure 3.7(b) displays the different contributions to the transport. The viscous and inertial components are nearly zero in the bulk and the pressure transport is the only effective contribution.

Approaching the wall, the production decreases and the dissipation grows, therefore the transport term becomes positive to balance the equation. The pressure and inertial components reach a maximum value within the boundary layer and become zero at the wall as the velocity fluctuations vanish at the boundary. The energy

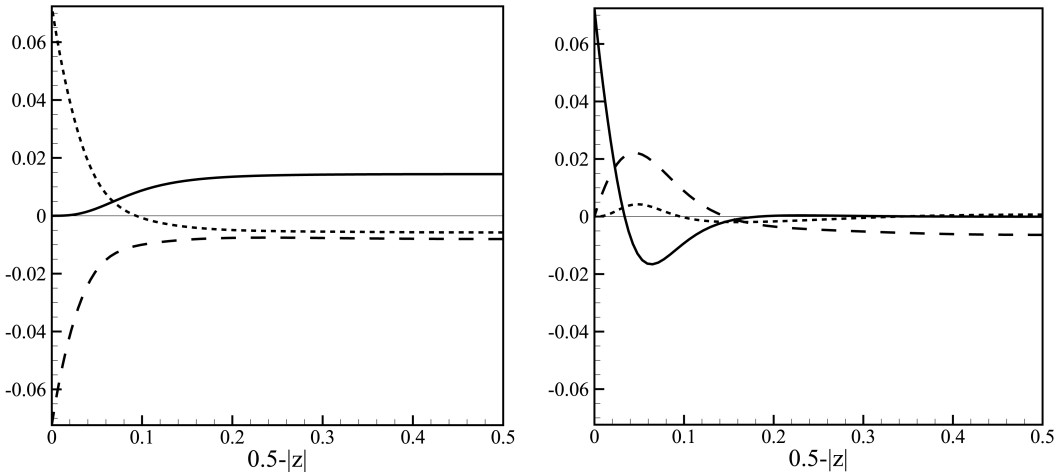

Figure 3.7: (a) Turbulent kinetic energy budget vs. distance from the wall $(0.5-|z|)$ for $Pr = 0.7$: production (solid line), total transport (dashed line) and dissipation (long-dashed line). (b) Different contributions to the transport vs. distance from the wall $(0.5-|z|)$: inertial transport (dashed line), pressure transport (long-dashed line) and viscous transport (solid line).

supplied by them is distributed within the boundary layer by the viscous transport, which is negative in the outer part of the boundary layer and positive in the inner part. Finally, the peak dissipation occurs at the wall, where the production is zero and the energy supply is provided only by the viscous transport.

Introducing the definition of the overall flux of turbulent kinetic energy,

$$\phi(z) = \langle kw \rangle + \left\langle wp^{'} \right\rangle - \sqrt{\frac{Pr}{Ra}} \frac{d\langle k \rangle}{dz}, \tag{3.15}$$

we can rewrite equation (3.14) as

$$\frac{d\phi}{dz} = \langle w\theta \rangle - \langle \tilde{\epsilon} \rangle \tag{3.16}$$

Figure 3.8 displays the different contributions to ϕ as a function of the distance from the wall and for $Pr = 0.7$. Where it is negative, the flux transfers energy toward the wall; where it is positive, the flux transfers energy toward the bulk. The peak flux occurs in the external part of the viscous boundary layer, where the overall transport of turbulent kinetic energy is equal to zero. For $0.5 - |z| < 0.1$ there is a sudden decrease of ϕ, which means that the energy coming from the bulk

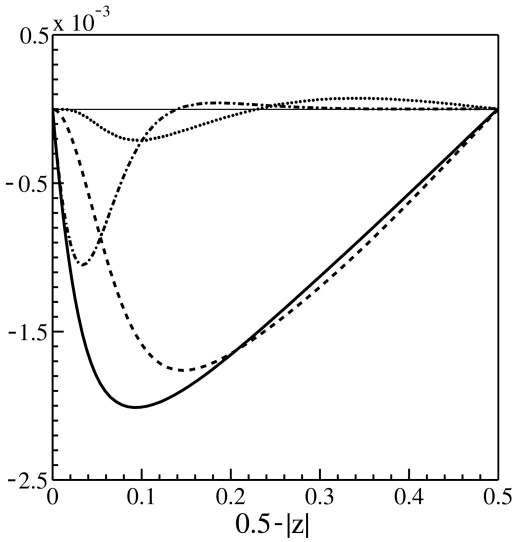

Figure 3.8: Different contributions to the flux ϕ as a function of the distance from the wall $(0.5 - |z|)$ for $Pr = 0.7$: inertial component (dots), pressure transport (dashed line), viscous transport (dashed-dotted line) and the total flux (solid line).

is intensely released inside the viscous boundary layer to balance the production decrease and the dissipation increase. As expected, the pressure contribution to the flux is dominant inside the bulk whereas it is negligible very close to wall. On the other hand, the inertial contribution is almost negligible everywhere and the viscous contribution is the most important one only very close to wall.

This picture of the flow confirms that the bulk plays the role of engine in turbulent Rayleigh-Bénard convection. Furthermore, the energy produced in the core region is sent toward the walls mainly by the pressure transport and finally it is dissipated close to the walls, where the viscous effects are dominant.

For the purpose of topological characterization, the others DNS do not add any relevant information, anyway it is important to study the dependence of the energy balance on the Prandtl number. In Figure 3.9 production and dissipation are plotted for the three values of Pr. It is concluded that production and the absolute value of dissipation decrease as Pr increases. This behaviour is strictly related to the Reynolds number characteristic of each simulation. Hence, as can be seen in Table 2.1, higher Pr corresponds to lower Re and, therefore, turbulence intensity decreases as Pr increases. Loosely speaking, velocity fluctuations are dampened efficaciously by high values of the kinematic viscosity, thus an higher Pr implies a lower production term $\langle w\theta \rangle$. Furthermore, the less energy is introduced in the flow,

the less energy is transported away from the bulk and dissipated close to the walls.

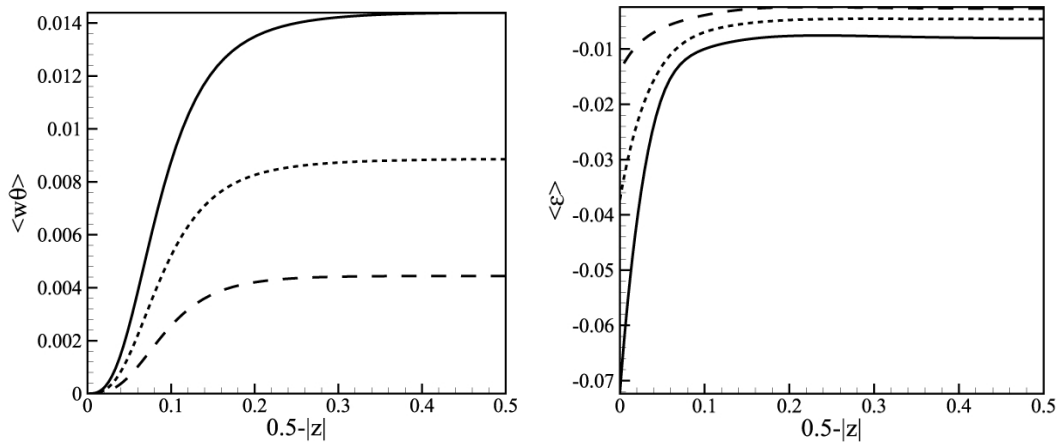

(a) (b)

Figure 3.9: Turbulent production (a) and dissipation (b) vs. distance from the wall $(0.5-|z|)$ for $Pr = 0.7$ (solid line), $Pr = 2$ (dashed line), $Pr = 7$ (long-dashed line).

3.4 Two-point correlations

In Section 3.1, a qualitative analysis of the coherent structures of the flow was attempted. Nevertheless, to draw conclusions about the characteristic length of the plumes, two-point statistics are needed. The simplest statistic containing some information on the spatial structure of the velocity and temperature fields is the two point, one-time autocovariance which is often referred to as the two-point correlation [22]. A correlation coefficient R_{ij} can be defined as

$$R_{ij}(\vec{\pi}, z, \vec{r}, t) = \frac{\langle u_i(\vec{\pi}, z, t) u_j(\vec{\pi} + \vec{r}, z, t) \rangle}{\sqrt{\langle u_i(\vec{\pi}, z, t) \rangle^2 \langle u_j(\vec{\pi} + \vec{r}, z, t) \rangle^2}}, \tag{3.17}$$

where $i, j = x, y, z$, $\vec{\pi} = (x, y)$ and $\vec{r} = (r_x, r_y)$ are respectively the position vector and the separation vector in the xy-plane at height z. Moreover, $u_i(x, y, z, t)$ is a generic vector field. Taking into account the statistical stationarity, the planar homogeneity and isotropy, the dependence of R_{ij} on both the position vector $\vec{\pi}$ and the direction of $\vec{r}$ vanishes, hence

$$R_{ij}(\vec{\pi}, z, \vec{r}) \to R_{ij}(z, r), \tag{3.18}$$

where $r = |\vec{r}|$. When $r = 0$, the correlation coefficient R_{ij} is, by definition, equal to one. At large r the fluctuations of $u_i(x, y, z, t)$ become independent of one another, therefore

$$\lim_{r\to\infty} \langle u_i(\vec{\pi}, z, t) u_j(\vec{\pi} + \vec{r}, z, t)\rangle = 0 \tag{3.19}$$

and R_{ij} asymptotically approaches zero. A correlation curve $R_{ij}(r)$ indicates the distance over which the motion at one point significantly affects that at another. It may be used to assign a length scale to the turbulence; a length can be defined for example as $\int_0^\infty R_{ij} dr$, or as the distance in which R_{ij} falls to $1/e$, or the value of r at which R_{ij} becomes zero [29].

Thermal plumes are coherent structures of the temperature field, which can be extracted from the flow using a threshold on both the temperature and the vertical velocity component. Hence, to evaluate the characteristic diameter of the plumes, the vertical velocity correlation coefficient R_{22} and the temperature correlation coefficient R are plotted as a function of the separation r (see Figures 3.10). Values

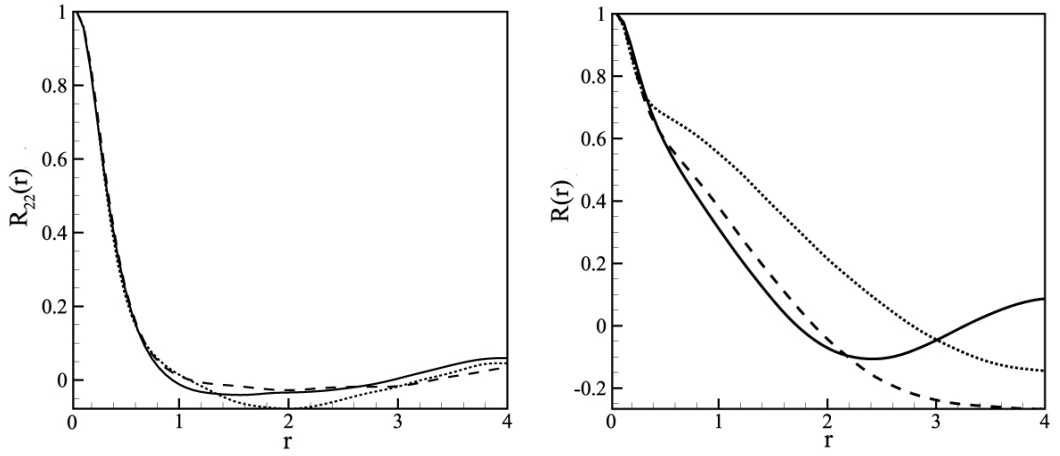

(a) (b)

Figure 3.10: (a) Vertical velocity correlation coefficient R_{22} and (b) temperature correlation coefficient R vs. the separation r for $Pr = 0.7$ (solid line), $Pr = 2$ (dashed-line) and $Pr = 7$ (dotted line).

above zero express a positive correlation, which means that as a variable increases in one point, the same variable in the other point increases too. That implies a link between the two points and, therefore, the presence of a coherent structure. Values equal to zero indicate a lack of correlation and the corresponding separation r could

represent the boundary of the coherent structure i.e. the diameter of the plume. As can be seen from Figure 3.10(a), the characteristic velocity-based diameter d_v is nearly equal to one in the center of the cell, independent of the Prandtl number. Furthermore, R_{22} reaches a positive peak at $r = 4$, which probably suggests that the coherent structures are separated by a distance $r \approx 4$. In relation to Figure 3.10(b), the following observation can be made. As Pr increases, both the temperature-based diameter d_t and the distance between two successive peaks, increase. The simulation at $Pr = 0.7$ is the only one that shows two distinct, positive correlated structures i.e. plumes having the same direction. In the horizontal slices through the centre, at $Pr = 2$ and $Pr = 7$, the mushroom-like plumes are wide and massive, and the domain seems not to be large enough to contain two positive correlated structures.

3.5 The generalized Kolmogorov equation

Turbulence is a multi-scale phenomenon, which means that in a generic point of the geometric domain, flow structures or eddies of various sizes coexists. Moreover, eddies range in size from the characteristic width of the flow, H, to much smaller scales, which become progressively smaller as the Reynolds number increases. An "eddy" eludes precise definition, but it is conceived to be a turbulent motion that is at least moderately coherent over a certain region [22].

The multi-scale feature poses a challenge in understanding turbulence because processes such as energy production, transport and dissipation depend both on the position in the geometric space x_i and on the turbulent scale considered r_i. For this reason the turbulent kinetic energy equation, introduced in Section 3.3, is insufficient to describe completely the turbulent dynamics because the balanced terms are single-point observable i.e. they depend on space coordinates but not on turbulent scales.

In this scenario, it is, therefore, necessary to provide a global approach. Appropriate candidates to consider for a simultaneous description of turbulent dynamics in physical and scale space are the two-points statistical observables, such as the second-order structure function for the velocity $\langle \delta u^2 \rangle (x_i, r_i)$ and the temperature $\langle \delta \theta^2 \rangle (x_i, r_i)$ [10], introduced in Section 1.2. As previously mentioned, these quantities can be thought as measures of the amount of kinetic and thermal energy, respectively, at scale $r = \sqrt{r_i r_i}$ and depend both on separation vector r_i and the

spatial location of the mid-point x_i, as sketched in Figure 3.11.

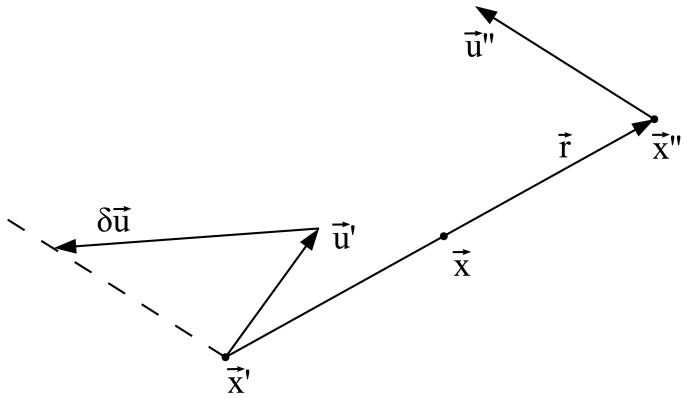

Figure 3.11: Sketch of the velocity difference between two points $\vec{x}$ and $\vec{x}''$: $\vec{r}$ is the separation vector, $\vec{x}$ is the midpoint of $\vec{r}$, $\vec{u}' = \vec{u}(\vec{x}')$, $\vec{u}'' = \vec{u}(\vec{x}'')$ and $\delta\vec{u} = \vec{u}'' - \vec{u}'$. The picture is partially based on a sketch in [20].

Using the equations for an incompressible flow, a balance for the second-order structure function $\langle \delta u^2 \rangle$, hereafter referred to as *scale energy*, can be derived. In the simplest case of stationary homogeneous isotropic turbulence i.e $\partial \langle \cdot \rangle / \partial x_i = 0$ and $\partial \langle \cdot \rangle / \partial r_x = \partial \langle \cdot \rangle / \partial r_y = \partial \langle \cdot \rangle / \partial r_z$, the following balance for the scale energy was proposed a long time ago by Kolmogorov in his famous 1941 papers [18] [17]

$$\frac{\partial \langle \delta u^2 \delta u_i \rangle}{\partial r_i} = -4 \langle \epsilon \rangle + \frac{2}{Re} \frac{\partial \langle \delta u^2 \rangle}{\partial r_i \partial r_i} + 2 \langle \delta f_i \delta u_i \rangle , \tag{3.20}$$

where $i = x, y, z$ and $\delta f_i(x_,r_i) = f_i(x_i + r_i/2) - f_i(x_i - r_i/2)$. Here, $f_i(x_i)$ is an external, statistically stationary and homogeneous forcing which effects only the largest scale of the system and supplies the kinetic energy lost by viscous dissipation. The term on the left hand side and the second term on the right hand side of equation (3.20) are respectively the inertial and the viscous contributions to the transport of scale energy in the space of scales, whereas the first and the last terms on the right hand side are, respectively, a sink and a source of scale energy, called dissipation and production. As can be noted, in homogeneous settings transport occurs only in the space of scales. There is no transport in the geometric domain, which is induced by inhomogeneity.

On the basis of equation (3.20), Kolmogorov developed in 1941 a phenomenological theory (K41) for the second-order velocity structure function. There are three hypotheses in the K41 theory. The first one, called the *local isotropy* hypothesis, is

an assumption of statistical homogeneity and isotropy of the small-scale turbulent motion ($r \ll H$) when the Reynolds number is sufficiently high and far from the boundaries. The second assumption, called the *first similarity* hypothesis, states that a range of scales $r \ll r_e$ exists, in which the statistics of δu_i are uniquely determined by the mean dissipation rate $\langle\epsilon\rangle$, the kinematic viscosity ν and the scale r, under the same conditions of the first assumption. The scale r_e is much less than H and represents the boundary between the isotropic and the anisotropic regimes of turbulence. Furthermore, the range $r \ll r_e$ is generally called *universal equilibrium range*. The last assumption, called the *second similarity* hypothesis, states that a range of intermediate scales $\eta \ll r \ll H$ exists in which the statistics of δu_i are uniquely and universally determined by the mean dissipation rate $\langle\epsilon\rangle$ and r, under the same conditions of the first assumption. This range of intermediate length scales is known as the *inertial range*.

In agreement with the Kolmogorov hypotheses, both the viscous contribution to the transport of scale energy and the production are negligible inside the inertial range, therefore equation (3.20) can be rewritten as

$$\frac{\partial \langle \delta u^2 \delta u_i \rangle}{\partial r_i} = -4 \langle \epsilon \rangle . \tag{3.21}$$

Considering the integration of equation (3.21) over a sphere B of radius $|\vec{r}|$ centered at $\vec{r} = 0$, equation (3.21) leads to

$$\int_{\partial B} \left\langle \delta u^2 \delta u_i \right\rangle \cdot \vec{n}_r dS = -\frac{4}{3} \langle \epsilon \rangle r, \tag{3.22}$$

where $\vec{n}_r$ is the outer normal to the sphere and the divergence theorem is used on the resulting volume integrals and it is divided by $2\pi r^2$. Since the flow considered here is isotropic, the integration over the sphere is redundant and relation (3.22) reduces to

$$\frac{\langle \delta u^2 \delta u_i \rangle r_i}{r} = -\frac{4}{3} \langle \epsilon \rangle r, \tag{3.23}$$

that gives the well-known K41 scaling, which predicts the statistical behaviour of inertial range turbulent velocity fluctuations

$$\delta u(r) \sim \langle \epsilon \rangle^{1/3} r^{1/3}. \tag{3.24}$$

Homogeneous and isotropic turbulence is quite uncommon in applications because it implies the absence of any solid boundary and any inhomogeneity in the mean velocity field, nevertheless it is a simple model for studying the dynamic of the chaotic fluid motion from a physical point of view. When dealing with wall-bounded turbulent flows, such as Rayleigh-Bénard convection, the statistical inhomogeneous condition and anisotropy has to be considered. Inhomogeneity increases the complexity of turbulent physics by introducing a spatial redistribution of energy and to a strong position-dependence of the turbulence dynamics. To deal with these more general conditions, the generalization of the Kolmogorov's approach to turbulence in the form of a balance equation for the second-order structure function, $\langle \delta u^2 \rangle$, can be used [10]. Following the procedure described for the first time by Hill [14] in 2002, it is possible to obtain from the Navier-Stokes equations the generalized form of the Kolmogorov equation for globally anisotropic and inhomogeneous conditions [20]

$$\begin{aligned} &\frac{\partial \langle \delta u^2 \rangle}{\partial t} + \frac{\partial \langle \delta u^2 \delta u_i \rangle}{\partial r_i} + \frac{\partial \langle \delta u^2 \delta U_i \rangle}{\partial r_i} + 2 \langle \delta u_i \delta u_j \rangle \frac{\partial \langle \delta U_j \rangle}{\partial r_i} + \frac{\partial \langle u_i^* \delta u^2 \rangle}{\partial x_i} + \\ &\frac{\partial \langle \delta u^2 U_i^* \rangle}{\partial x_i} + 2 \langle u_i^* \delta u_j \rangle \frac{\partial \langle \delta U_j \rangle}{\partial x_i} = -4 \langle \tilde{\epsilon}^* \rangle + \frac{2}{Re} \frac{\partial \langle \delta u^2 \rangle}{\partial r_i \partial r_i} - 2 \frac{\partial \langle \delta p \delta u_i \rangle}{\partial x_i} + \\ &\frac{1}{2Re} \frac{\partial^2 \langle \delta u^2 \rangle}{\partial x_i \partial x_i}, \end{aligned} \tag{3.25}$$

where the asterisk denotes the mid-point average

$$\beta^* = \frac{\beta(x_i'') + \beta(x_i')}{2}, \tag{3.26}$$

for a generic variable β, where $x_i' = x_i - r_i/2$ and $x_i'' = x_i + r_i/2$. This evolution equation allows to identify all the processes which characterize the dynamics of inhomogeneous anisotropic flows both in the space of scales and in the physical space. In particular, the terms with r-derivatives describe physical processes which transfer energy through scales while those with x-derivatives arise due to inhomogeneities and describe physical processes which transfer energy through different regions of the flow [10]. When homogeneous and isotropic conditions are reached, the generalized Kolmogorov equation reduces to the classical Kolmogorov equation (3.20) with the exception of $2 \langle \delta f_i \delta u_j \rangle$, which is "artificially" added to the Kolmogorov equation to

supply energy and preserve the temporal invariance of the system.

Next, we show how to specialize equation (3.25) to the turbulent Rayleigh-Bénard convection. Horizontal isotropy and homogeneity yield $\partial \langle \cdot \rangle / \partial x = \partial \langle \cdot \rangle / \partial y = 0$ and, together with the no-slip conditions at the top and bottom plates, $\langle U_i \rangle = 0$. When the flow is in the stationary state, $\partial \langle \cdot \rangle / \partial t$ vanishes. Finally, the term $2\langle \delta\theta \delta w \rangle$ is included to take into account the production of scale energy due to buoyancy forces. Thus we get

$$\begin{aligned} \frac{\partial \langle \delta u^2 \delta u_i \rangle}{\partial r_i} + \frac{\partial \langle w^* \delta u^2 \rangle}{\partial z} = -4 \langle \tilde{\epsilon}^* \rangle + 2\sqrt{\frac{Pr}{Ra}} \frac{\partial^2 \langle \delta u^2 \rangle}{\partial r_j \partial r_j} \\ -2\frac{\partial \langle \delta p \delta w \rangle}{\partial z} + \frac{1}{2}\sqrt{\frac{Pr}{Ra}} \frac{\partial^2 \langle \delta u^2 \rangle}{\partial z^2} + 2\langle \delta\theta \delta w \rangle, \end{aligned} \tag{3.27}$$

where $Re = \sqrt{Ra/Pr}$.

Equation (3.27) manifests a well-defined asymptotic behaviour as larger and larger scales are approached. For $r \gg l$, where l is the relevant correlation length, quantities evaluated at x_i' and x_i'' are uncorrelated and equation (3.27) reduces, within a factor four, to the mid-point average of the single-point energy budget (3.14) [20]. For example, the large scale limit of the inertial transport in the space of scales is

$$\lim_{r\to\infty} \frac{\partial \langle \delta u^2 \delta u_i \rangle}{\partial r_i} = \frac{1}{2}\left(\frac{\partial \langle u'^2 u_i' \rangle}{\partial x_i'} + \frac{\partial \langle u''^2 u_i'' \rangle}{\partial x_i''} \right) = \frac{\partial \langle u^2 u_i \rangle^*}{\partial x_i} = \frac{\partial \langle u^2 w \rangle^*}{\partial z}, \tag{3.28}$$

where $u_i' = u_i(x_i')$ and $u_i'' = u_i(x_i'')$ as sketched in Figure 3.11. The following rules for the transformation of the derivatives have been used

$$\frac{\partial}{\partial r_i} = \frac{1}{2}\left(\frac{\partial}{\partial x_i''} - \frac{\partial}{\partial x_i'} \right), \qquad \frac{\partial}{\partial x_i} = \frac{1}{2}\left(\frac{\partial}{\partial x_i''} + \frac{\partial}{\partial x_i''} \right). \tag{3.29}$$

It can be demonstrated that the large scale limit of the inertial transport in the geometric space is

$$\lim_{r\to\infty} \frac{\partial \langle w^* \delta u^2 \rangle}{\partial z} = \frac{\partial \langle u^2 w \rangle^*}{\partial z}. \tag{3.30}$$

Relation (3.28) and (3.30) reveal that both the contributions, in the space of scales and physical space, to the transport of turbulent kinetic energy are present with

the same value in the turbulent kinetic energy equation. Therefore, the single-point transport of turbulent kinetic energy represents the large scale boundary condition for the corresponding terms in the generalized Kolmogorov equation [10].

Rearranging equation (3.27) in order to group all the terms together on the left hand side and, then, averaging over a circle C of radius r belonging to xy parallel planes since we are homogeneous and isotropic in the xy-plane, we obtain the so called r-averaged form of equation (3.27)

$$T_c(r,z) + P(r,z) + D_c(r,z) + T_r(r,z) + D_r(r,z) + \Pi(r,z) + E(r,z) = 0, \quad (3.31)$$

where

$$\begin{gathered} T_c = -\frac{1}{\pi r^2}\int_{C(r)} \frac{\partial \langle w^* \delta u^2 \rangle}{\partial z} dxdy, \qquad P = -\frac{2}{\pi r^2}\int_{C(r)} \frac{\partial \langle \delta p \delta w \rangle}{\partial z} dxdy \\ D_c = \frac{1}{2\pi r^2}\sqrt{\frac{Pr}{Ra}}\int_{C(r)} \frac{\partial^2 \langle \delta u^2 \rangle}{\partial z^2} dxdy. \end{gathered} \quad (3.32)$$

are respectively the inertial, the pressure-velocity and the viscous contributions to the transport of scale-energy in geometric space, which arises from the inhomogeneous condition. Furthermore

$$T_r = -\frac{1}{\pi r^2}\int_{C(r)} \frac{\partial \langle \delta u^2 \delta u_i \rangle}{\partial r_i} dxdy, \qquad D_r = \frac{2}{\pi r^2}\sqrt{\frac{Pr}{Ra}}\int_{C(r)} \frac{\partial^2 \langle \delta u^2 \rangle}{\partial r_j \partial r_j} dxdy, \quad (3.33)$$

are, in order, the inertial and the viscous contributions to the transport of scale energy in the space of scales, and finally

$$\Pi = \frac{2}{\pi r^2}\int_{C(r)} \langle \delta\theta \delta w \rangle dxdy, \qquad E = -\frac{4}{\pi r^2}\int_{C(r)} \langle \tilde{\epsilon}^* \rangle \, dxdy, \quad (3.34)$$

are the production and dissipation of scale energy, respectively.

The generalized Kolmogorov equation directs the attention to the energy content of a given scale r of turbulent motion as a function of the z-coordinate, allowing us to display the processes occurring simultaneously in the space of turbulent scales and in the physical space. To streamline the notation, the overall transport in the

geometric space and in the space of the scales, respectively $\widetilde{T}_c$ and $\widetilde{T}_r$, are introduced

$$\widetilde{T}_c(r,z) = T_c(r,z) + P(r,z) + D_c(r,z), \qquad \widetilde{T}_r(r,z) = T_r(r,z) + D_r(r,z), \tag{3.35}$$

thus we can rewrite equation (3.31) as

$$\widetilde{T}_c(r,z) + \widetilde{T}_r(r,z) + \Pi(r,z) + E(r,z) = 0. \tag{3.36}$$

We start by giving a physical interpretation of this balance. Let us consider the eddies of different sizes filling an horizontal plane at height z of the convection cell (see Figure 3.12 (left)). This picture agrees with the Richardson's view of turbulence [24], in which turbulent flows are composed by eddies of different size r and these eddies are superimposed i.e. large structures contain smaller structures. Statistically, these eddies can be organized into a set of concentric circles of radius r, as sketched in Figure 3.12 (right). The largest and the smallest eddies correspond respectively to the outmost and the innermost circle whereas the intermediate structures are represented by in-between circles.

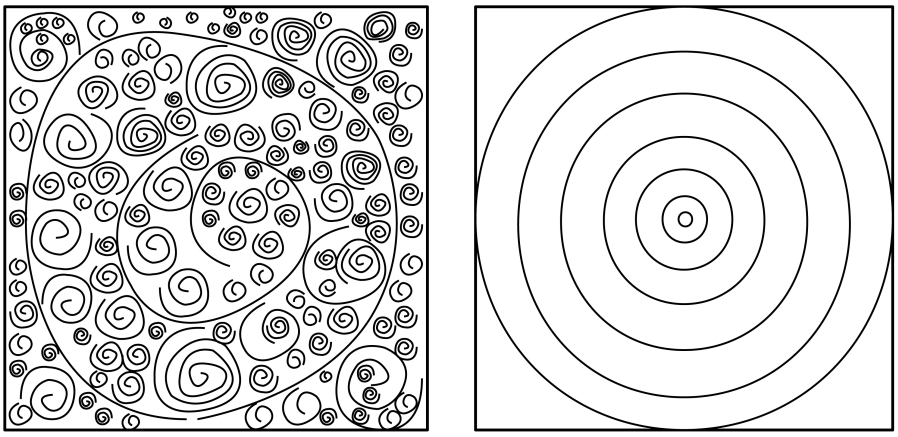

Figure 3.12: Left: sketch of multi-scale eddies in a horizontal plane of the cell. Right: conceptual representation of the eddy-hierarchy.

Now, we consider the energy budget (3.36) at the largest scale of turbulent motion. For r much greater than the relevant correlation length, the generalized Kolmogorov equation reduces, within a factor four, to the turbulent kinetic energy equation, therefore, at the largest scale, the energy balance to be considered is simply the turbulent kinetic energy equation (3.14), which is represented in the first sketch from left of Figure 3.13. As can be seen, the more energy enters the largest scale of

turbulence (red arrow) by production and spatial transport mechanisms, the more it is dissipated within it (purple arrow).

To specify the generalized Kolmogorov equation for smaller scales, the outer shells of our stratified model must be "peeled away" and substituted by a term accounting for the larger scales just removed, which are represented by dashed lines in Figure 3.13. This term, indicated by yellow arrows in Figure 3.13, is the overall transport in the space of scales $\tilde{T}_r$. If $\tilde{T}_r$ is positive, the outer scales supply energy to the inner one and the so-called *direct cascade* of energy takes place. On the other hand, if $\tilde{T}_r$ is negative, the outer scales subtracts energy from the inner one, meaning that a *reverse cascade* process occurs.

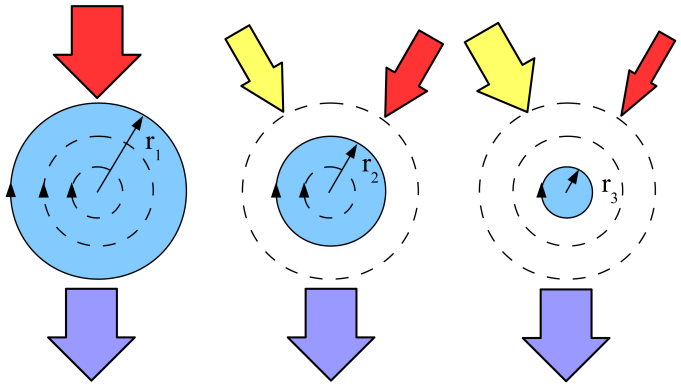

Figure 3.13: Sketch of the energy balance at different scales. The colored arrows represent the sum $\Pi + \widetilde{T}_c$ (red arrows), the dissipation $-E$ (purple arrows) and the overall transport in the r-space $\tilde{T}_r$ (yellow arrows).

The idea of the direct energy cascade was theorised for the first time by Richardson in 1922 [24]. According to Richardson's intuition, the kinetic energy enters turbulence at the largest structures of turbulent motion, where the effects of viscosity are negligible. These eddies are unstable and break down, transferring their energy by nonlinear interaction toward smaller eddies. This process continues until the length scales involved are associated with velocity gradients sufficiently large to give an appreciable viscous dissipation of kinetic energy into heat. On the other hand, the transfer of scale energy from small to large scales is called inverse energy cascade. This phenomenon occurs when the kinetic energy is injected into the turbulence at small scales, which cluster and merge together into larger ones. This means that energy is gradually transferred from small to large scales by consecutive coalescent events [10].

3.5.1 Spatial redistribution of energy

We are now ready to analyse the DNS results. In this section, we consider the generalized Kolmogorv equation at fixed scales to understand how the scale energy redistributes in the geometric domain for different values of r. Figure 3.14(a) displays the production term $\Pi(r, z)$ as a function of the distance from the wall $0.5 - |z|$ for different values of the scale r, at $Pr = 0.7$. In the same figure, the solid line corresponds to four times the production of turbulent kinetic energy ($4 \langle w\theta \rangle$), plotted as a function of the distance from the wall. As can be seen, the production of scale-energy is concentrated at high r and $\Pi(r, z) \to 4 \langle w\theta \rangle$ when $r \to \infty$, supporting the theoretical prediction made in the previous section.

The overall transport of scale energy in the geometric space $\widetilde{T}_c$ is plotted in Figure 3.14(b). As r increases, $\widetilde{T}_c$ increases inside the viscous boundary layer and decreases in the bulk. Similarly to the single point-energy budget, the negative value of the transport indicates the extraction and the positive values indicates the supply of energy to the respective region. At small scale ($r = 0.25$), $\widetilde{T}_c$ is positive inside the viscous boundary layer, negative in the internal portion of the bulk ($0.1 < 0.5 - |z| < 0.3$) and equal to zero in the external one ($0.3 < 0.5 - |z| < 0.5$). At larger scales, $\widetilde{T}_c$ remains positive inside the viscous boundary layer and becomes entirely negative in the bulk. This means that the spatial transfer of scale energy from the bulk toward the near-wall region affects particularly the larger scales. This behaviour is in accordance with the Kolmogorov first hypothesis, in the sense that the local isotropy should be recovered at sufficiently small scales and, therefore, only large eddies should be anisotropic and thus responsible for the spatial transfer of scale energy [20].

The fundamental term introduced in the generalized Kolmogorov equation is the transport of scale energy in the r-space, $\widetilde{T}_r$. As it can be seen from Figure 3.14(c), at large scales, $\widetilde{T}_r$ is zero in the bulk, then it becomes negative in the external part of the viscous boundary layer and, finally, positive at the wall. Furthermore, as r decreases, the $\widetilde{T}_r$ profiles move up and become positive. In confirmation of the asymptotic behaviour of the generalized Kolmogorov equation, it can be seen in Figure 3.14(b) that, in the large scale limit, the sum $\widetilde{T}_c + \widetilde{T}_r$ converges to four times the overall transport of turbulent kinetic energy, which is represented by solid line in Figure 3.14(b).

The others DNS do not add any relevant information in the sense that the same

characteristic behaviour at different scales is seen, therefore they are not reported.

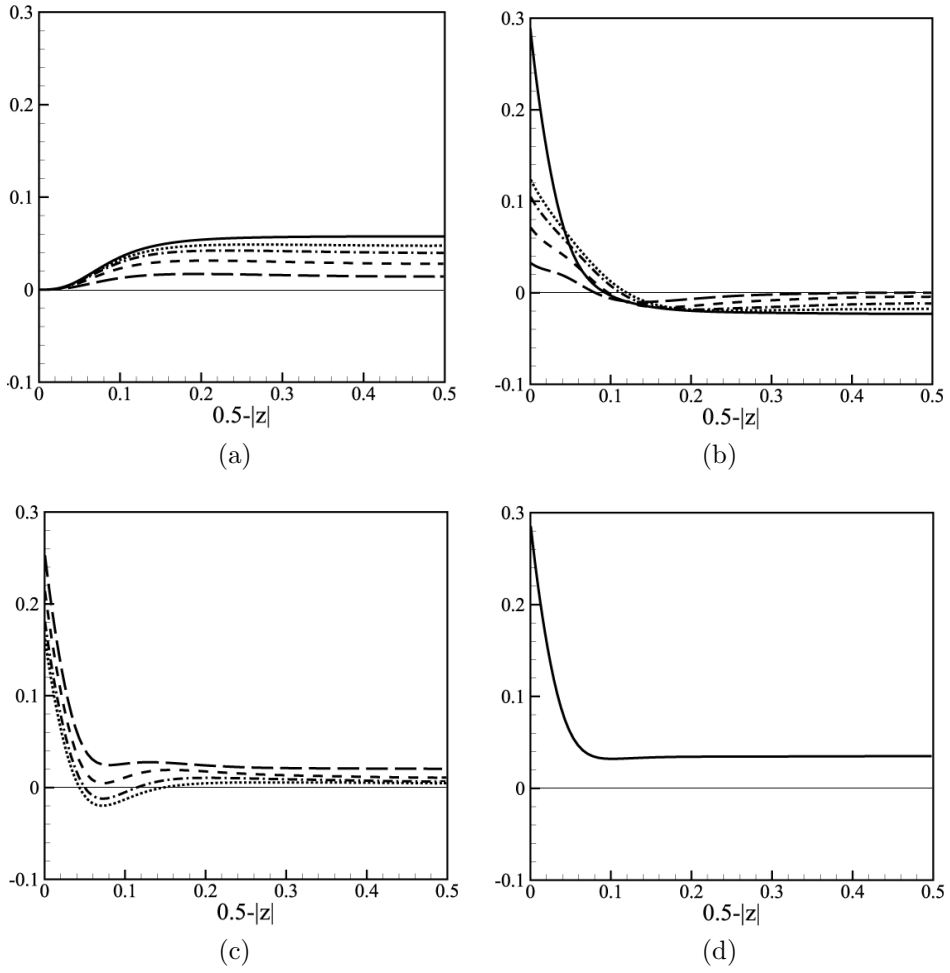

Figure 3.14: Terms of the generalized Kolmogorov equation vs. distance from the wall ($0.5 - |z|$) for $r = 0.25$ (long-dashed line), $r = 0.5$ (dashed line), $r = 0.9$ (dashed-dot line), $r = 1.25$ (dotted line): (a) production Π, (b) overall transport in the geometric space $\widetilde{T}_c$, (c) overall transport in the r-space $\widetilde{T}_r$, (d) dissipation $-E$. In (a) and (b), the solid line represents, respectively, four times the production and transport of turbulent kinetic energy.

3.5.2 Scale-by-scale budget

We analyze now the dependence on r of the generalized Kolmogorov balance at fixed z. To that end, equation 3.31 can be recast in a simple form

$$\widetilde{T}_r(r,z) + \widetilde{\Pi}(r,z) + E(r,z) = 0, \tag{3.37}$$

to be read as: effective production plus transfer across scales equals dissipation. The term $\widetilde{\Pi} = T_c + P + D_c + \Pi$ is the effective production, that is the amount of scale energy which is effectively available at a given geometric location z. The single contributions to the effective production are not positive definite, while their sum must be positive since it represents the only production mechanism of the flow.

The simulations results are organized as follows: Figure 3.15 and 3.16 show the terms of balance (3.37) at several locations in the near-wall region for the $Pr = 0.7$ and the $Pr = 7$ simulations respectively, whereas Figure 3.17 focuses on the center for both the $Pr = 0.7$ and the $Pr = 7$ simulations. The scale-by-scale budget for the $Pr = 2$ simulation do not add any relevant information, therefore it is not reported.

We start by analyzing the balance at $Pr = 0.7$. As can be seen in Figure 3.15(a), next to the wall ($0.5 - |z| = 0.02$), the dissipation exceeds the effective production at every scale, hence a positive transfer across scales develops to balance the equation and a direct energy cascade is observable. The scenario changes radically at a distance from the wall slightly above 0.02.

Figure 3.15 (b) shows the scale-by-scale budget at $0.5 - |z| = 0.04$: as can be seen, for $r < 1.3$ the effective production is less than the dissipation, whereas for $r > 1.3$ the effective production exceeds the dissipation. This energy excess leads to both a reverse and a direct cascade; indeed the transfer term $\widetilde{T}_r$ shows both positive and negative values. As sketched in Figure 3.18, the effective amount of energy which is available at large scales can not be entirely transferred toward smaller scales since $\widetilde{\Pi} > -E$ and the smallest scales are demanded to dissipate an amount of energy equals to E. This means that the direct cascade of energy has reached its maximum drain capability and the energy excess, $\widetilde{\Pi} + E$, can only move towards larger scales, entailing a reverse energy cascade. The amount of energy that reaches large scales due to the reverse cascade cannot be entirely dissipated because viscous effects are negligible for $r \gg 1$. Hence, a spatial flux of energy is developed, so that the scale energy can be transported away through the spatial domain ($\widetilde{T}_c < 0$),

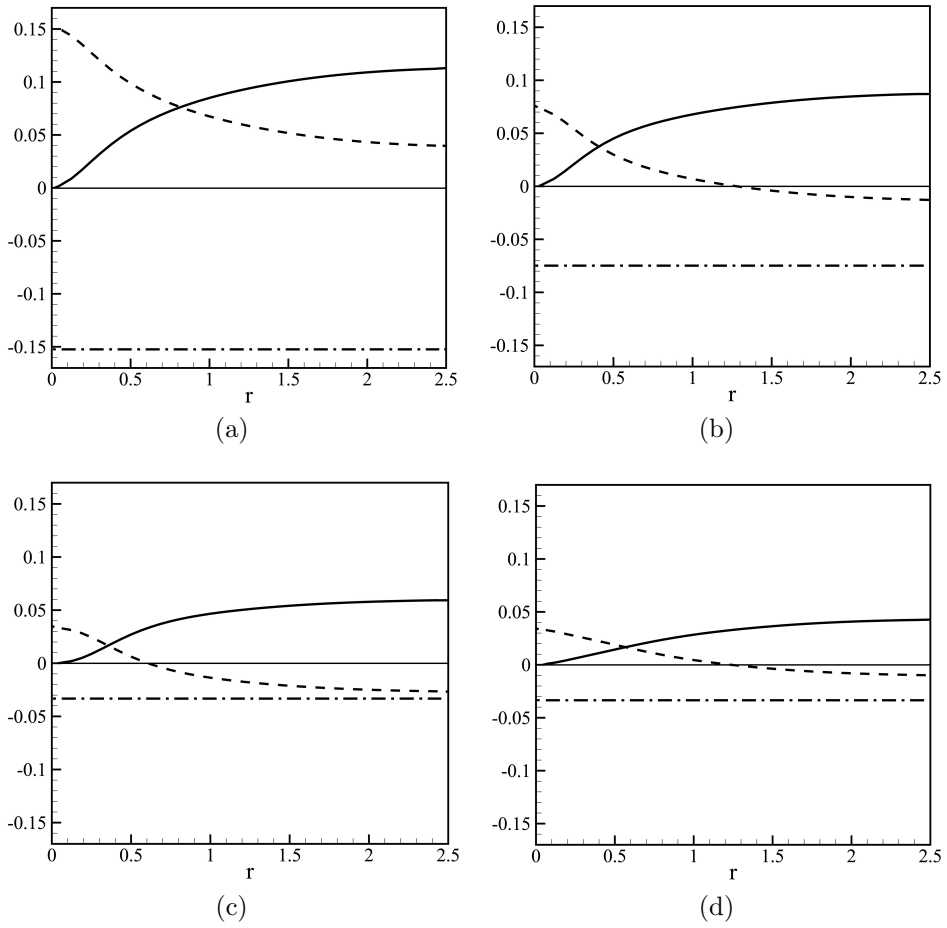

Figure 3.15: Effective production $\widetilde{\Pi}$ (solid line), transport of scale energy in the r-space $\widetilde{T}_r$ (dashed line) and dissipation E plotted as function of r in the near-wall region at $0.5 - |z| = 0.02$ (a), $0.5 - |z| = 0.04$ (b), $0.5 - |z| = 0.08$ (c) and $0.5 - |z| = 0.14$ (d). Results from the $Pr = 0.7$ DNS.

keeping the statistical stationarity of the flow. The scenario changes at small scales, where effective production alone is not sufficient to sustain the direct cascade which leads to dissipation, therefore larger scales must feed the smaller scales with energy, entailing a direct cascade.

The double cascade is still observable in Figure 3.15(c) and (d): in regards to this behaviour, it is important to notice that between $0.5-|z| = 0.04$ and $0.5-|z| = 0.08$, the range of scales in which the reverse cascade takes place becomes larger and reaches a maximum. Furthermore, as the distance from the wall increases, the direct cascade tends to re-establish as can be seen by comparing Figure 3.15(c) with

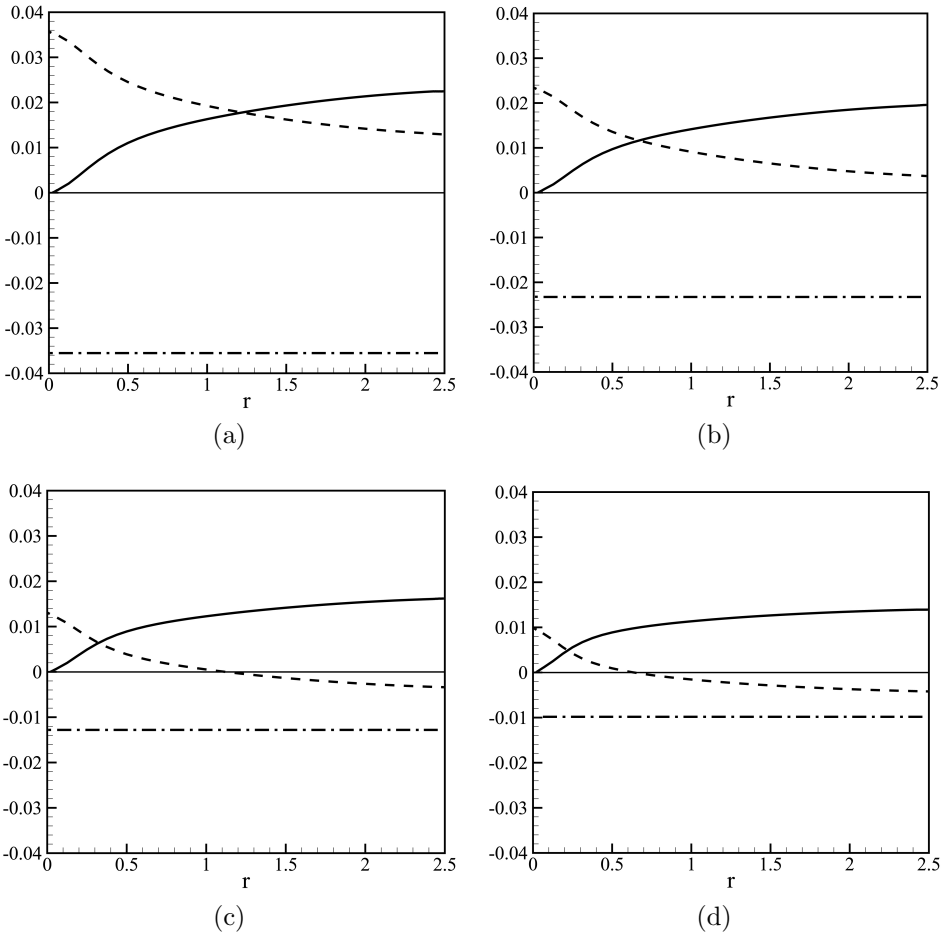

Figure 3.16: As Figure 3.15 but for the $Pr = 7$ simulation.

Figure 3.15 (d) and 3.17 (a).

By comparing the balance at $Pr = 0.7$ with the one at $Pr = 7$, two observations can be made. First of all, the effective production, the dissipation and, consequently, the transport of scale energy in the r-space, all evaluated at $Pr = 7$, are one order of magnitude less than their equivalents at $Pr = 0.7$. The fact that, as Pr increases, the intensity of turbulence decreases, is is strictly related to the Reynolds number characteristic of each simulation. Hence, as can be seen in Table 2.1, higher Pr corresponds to lower Re and, therefore, turbulence intensity decreases as Pr increases. The second and most import observation is that, for $Pr = 7$, the maximum range of scales assigned to the reverse cascade is observable at a distance from the wall which is much larger as compared with the case at $Pr = 0.7$. Indeed for $Pr = 7$, the range of scales in which the reverse cascade takes place has not a maximum between

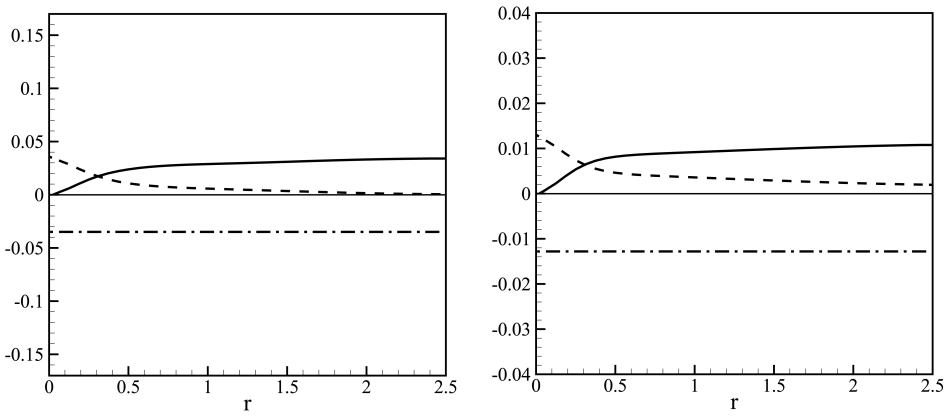

(a) (b)

Figure 3.17: As Figure 3.15 but at $(0.5 - |z|) = 0.5$, for $Pr = 0.7$ (a) and $Pr = 7$ (b).

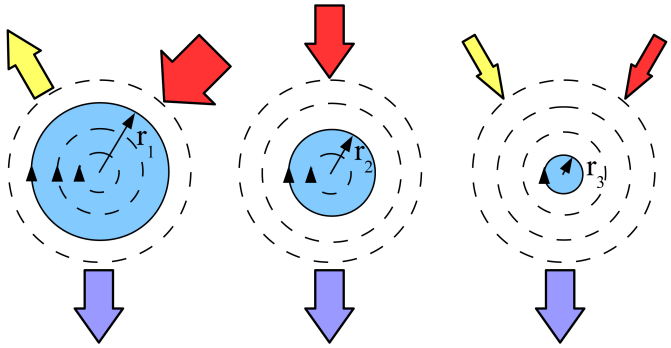

Figure 3.18: Sketch of the energy balance represented in Figure 3.15 (b), (c) and (d) and Figure 3.16 (c) and (d). The colored arrows represent the effective production (red arrows), the dissipation $-E$ (purple arrows) and the overall transport in the r-space (yellow arrows).

$0.5 - |z| = 0.04$ and $0.5 - |z| = 0.08$ like $Pr = 0.7$ simulation, but at distance from the wall greater than $0.5 - |z| = 0.08$.

It remains to be understood how the inverse cascade can be explained in terms of coherent structures. The main clue is the location of the phenomenon as function of the Prandtl number. By recalling Figure 3.6, which displays the viscous boundary layer thickness at different Pr, we can claim that the inverse cascade is very strong in the external part of the viscous boundary layer. The effect of plume impingement is dominant in this particular region, as can be seen in the instantaneous temperature and velocity fields displayed in Figure 3.1, 3.2 and 3.3. Hot and cold plumes detach

from their respective thermal boundary layers, move into the bulk of the cell and finally impinge on the opposite viscous boundary layer. Following on from the impact, thermal plumes spread out and organise into larger structures, therefore, the scale energy localized into plumes flows upwards and a reverse cascade develops.

Chapter 4

Concluding remarks

A numerical study of turbulent Rayleigh-Bénard convection is the main purpose of this thesis. By analyzing the results from three direct numerical simulations at $Ra \approx 10^5$ and $Pr = \{0.7, 2, 7\}$ with many statistical tools, a detailed picture of convective turbulence is shown. Similarly to other wall-bounded flows, turbulent Rayleigh-Bénard convection presents anisotropies and coherent structures formations close to the walls and nearly isotropic turbulence in the bulk. The temperature field plays a fundamental role in the near-wall region, where large thermal gradients trigger the detachment of fluid portions from the boundary layers, called plumes, which move toward the center carrying a large amount of thermal energy. Through the bulk, the thermal plumes are accelerated by buoyancy forces and a large amount of turbulent kinetic energy is produced within the flow. Furthermore, the turbulent kinetic energy is transported toward the near-wall region by the plumes and is finally dissipated inside the viscous boundary layer, induced by the large-scale circulation. This picture emerges by analyzing the simulation results with both one-point statistics (mean, variance and one-point energy budget) and two-point statistics (correlations and Kolmogorov equation). Moreover, a relation between two fundamental coherent structures of turbulent Rayleigh-Bénard convection, the thermal plume and the large-scale circulation, can be reasonably seen by analyzing the generalized Kolmogorov equation. In particular, it has been proposed that the impingement of thermal plumes leads to the formation of larger structures, such as the large-scale circulation. The main evidence supporting this phenomenological explanation is the presence of a reverse cascade of energy only in the near-wall region, where the effect of plume impingement is dominant. To conclude, the fact that a

reverse cascade has been identified has a direct effect on future attempts to model the effects of small-scale motions in turbulent Rayleigh-Bénard convection.

Appendix A

Exact relations

Using the dimensional Oberbeck-Boussinesq equations (2.9) and the boundary conditions (2.12), two exact relations for the mean dissipation rate of turbulent kinetic energy $\langle\epsilon\rangle$ and temperature $\langle\chi\rangle$, can be derived [8]. Taking the scalar product of equation (2.9b) for U_i and taking the scalar product of equation (2.9c) for Θ, and then, averaging over the volume of the cell and time, $\langle\cdot\rangle_{V,t}$, we obtain

$$\frac{1}{2}\frac{d}{dt}\langle U_i U_i\rangle_{V,t} + \frac{1}{2}\left\langle U_j \frac{\partial\left(U_i U_i\right)}{\partial x_j}\right\rangle_{V,t} = -\frac{1}{\rho_0}\left\langle U_i \frac{\partial p^*}{\partial x_i}\right\rangle_{V,t} + \nu\left\langle U_i \frac{\partial^2 U_i}{\partial x_j \partial x_j}\right\rangle_{V,t} + \alpha g \langle U_i \Theta\rangle_{V,t}\,\delta_{iz}, \tag{A.1}$$

$$\frac{1}{2}\frac{d}{dt}\left\langle\Theta^2\right\rangle_{V,t} + \frac{1}{2}\left\langle U_j \frac{\partial\Theta^2}{\partial x_j}\right\rangle_{V,t} = \kappa\left\langle\Theta\frac{\partial^2\Theta}{\partial x_j\partial x_j}\right\rangle_{V,t} = \frac{\kappa}{2}\left\langle\frac{\partial^2(\Theta^2)}{\partial x_j\partial x_j}\right\rangle_{V,t} - \kappa\left\langle\frac{\partial\Theta}{\partial x_j}\frac{\partial\Theta}{\partial x_j}\right\rangle_{V,t}. \tag{A.2}$$

The flow is assumed statistically stationary i.e. $d\langle\cdot\rangle_{V,t} = 0$. Using the continuity equation (2.9a) and the no-slip boundary condition at the walls, we can rewrite equation (A.1) and (A.2) in the following way

$$\nu\left\langle\frac{\partial U_i}{\partial x_j}\frac{\partial U_i}{\partial x_j} + \frac{\partial U_j}{\partial x_i}\frac{\partial U_i}{\partial x_j}\right\rangle_{V,t} = -\alpha\langle U_i f_i \Theta\rangle_{V,t}, \tag{A.3a}$$

$$\kappa\left\langle\frac{\partial\Theta}{\partial x_j}\frac{\partial\Theta}{\partial x_j}\right\rangle_{V,t} = \frac{\kappa}{2}\left\langle\frac{\partial^2(\Theta^2)}{\partial x_j\partial x_j}\right\rangle_{V,t}, \tag{A.3b}$$

where the two terms on the left hand side are, in order, $\langle\epsilon\rangle_{V,t}$ and $\langle\chi\rangle_{V,t}$. Applying the divergence theorem gives

$$\begin{aligned}\frac{\kappa}{2}\left\langle\frac{\partial^2(\Theta^2)}{\partial x_j\partial x_j}\right\rangle_{V,t} &= \kappa\left\langle\frac{\partial}{\partial x_j}\left(\Theta\frac{\partial\Theta}{\partial x_j}\right)\right\rangle_{V,t} = \frac{\kappa}{H}\int_{-H/2}^{H/2}\left\langle\frac{\partial}{\partial z}\left(\Theta\frac{\partial\Theta}{\partial z}\right)\right\rangle_t dz \\ &= \frac{\kappa}{H}\left[\left\langle\Theta\frac{\partial\Theta}{\partial z}\right\rangle_{z=H/2,t} - \left\langle\Theta\frac{\partial\Theta}{\partial z}\right\rangle_{z=-H/2,t}\right], \end{aligned} \tag{A.4}$$

where

$$\left\langle\Theta\frac{\partial\Theta}{\partial z}\right\rangle_{z=H/2,t} = -\left\langle\Theta\frac{\partial\Theta}{\partial z}\right\rangle_{z=-H/2,t} = \frac{\phi}{2\kappa} = \frac{Nu}{H}\frac{\Delta T}{2}. \tag{A.5}$$

Here, ϕ is the heat flux through the top and the bottom walls. Finally, the following exact relations for $\langle\epsilon\rangle_{V,t}$ and $\langle\chi\rangle_{V,t}$ can be written

$$\langle\epsilon\rangle_{V,t} = \alpha g\kappa\frac{\Delta T}{H}(Nu-1) = \frac{\nu\kappa^2}{H^4}Ra(Nu-1), \tag{A.6a}$$

$$\langle\chi\rangle_{V,t} = \frac{\kappa\Delta T^2}{H^2}Nu. \tag{A.6b}$$

Appendix B

Eduction of coherent structures

In the previous chapters, the dynamics of the "coherent structures" has been considered. An open problem remains in the identification of these structures that is not always univocal. In fact, a first step towards a better understanding of the physics of turbulent motions should pass by an unambiguous way to identify the flow structures.

As far as thermal plumes are concerned the solution is quite simple, since they can be easily identified using the isocontours of temperature or vertical velocity component.

For the identification of the vortices the matter is more complex and is still under discussion. The method used in this work is the one introduced by Cantwell [9], based on the signs of the eigenvalues of the velocity gradient. In this approach vortices are defined as regions where the rotation prevails over the local strain, allowing for a spiralling motion of the particles. The existence of a vortical structure is related to the local kinematic field. Hence, in order to characterise the relative motion in a given part of the field, the velocity gradient tensor is studied. In fact the equation for the relative motion vector ($r = x - x_0$) is the following

$$\frac{dr_i}{dt} = \frac{\partial u_i}{\partial x_j} r_i = A_{ij} r_j. \tag{B.1}$$

At each point a linearised problem can be considered and hence the trajectory of the relative motion is determined by the eigenvalues λ_1, λ_2 and λ_3 of the velocity

gradient which are the solution of the characteristic equation

$$\lambda^3 + P\lambda^2 + Q\lambda + R = 0. \tag{B.2}$$

The coefficients of this polynomial equation are the invariants of the velocity gradient which are equal to

$$P = -A_{ii} \qquad Q = -\frac{1}{2} A_{ij} A_{ji} \qquad R = -\frac{1}{3} A_{ij} A_{jk} A_{ki} \tag{B.3}$$

where the first invariant P is identically equal to zero for incompressible flows. It can be shown that the nature of the roots is determined by the sign of the discriminant

$$D = \frac{27}{4} R^2 + Q^3. \tag{B.4}$$

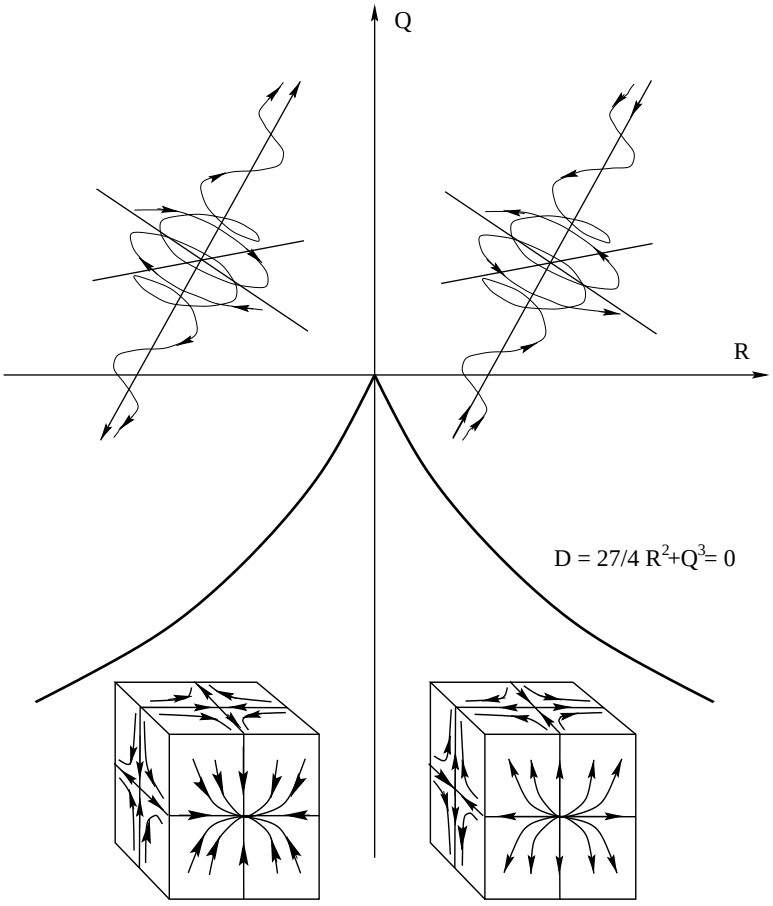

Figure B.1: Summary of the possible topologies.

If the discriminant is positive the tensor A_{ij} admits two complex conjugate eigenvalues and a real one, whereas if $D < 0$ there are three real eigenvalues. This means that since there is spiralling motion when there are complex conjugate eigenvalues the condition for the existence of vortices is $D > 0$. Because of incompressibility the sum of the three eigenvalues must be equal to zero, hence there is at least an eigenvalue of each sign. The division between positive and negative is determined by the sign of $R = -\lambda_1\lambda_2\lambda_3$, so if $R > 0$ there is one direction of contraction and two of expansion, if $R < 0$ there is one direction of expansion and two of contraction. A summary of the possible situations is shown in Figure B.1.
The second invariant can be split is two terms

$$Q = -\frac{1}{2}\left(S_{ij}\,S_{ji} + \Omega_{ij}\,\Omega_{ji}\right) \tag{B.5}$$

this expression underlines the fact that the local flow pattern depends on the balancing between vorticity and strain. Hence regions where the vorticity prevails on the strain component of the velocity gradient, positive values of Q, correspond to positive values of the discriminant. Zones characterised by a high vorticity present spiralling motion. In this view, we will identify as vortices regions of the turbulent boundary layer where the discriminant is positive. An important feature of this method is that both Q and R, and consequently the discriminant, are invariant under non-uniform translations and are independent of the orientation of the coordinate transformation.

Bibliography

[1] G. Ahlers. Turbulent convection. *Physics*, 2:74, Sep 2009.

[2] G. Ahlers, S. Grossmann, and D. Lohse. Heat transfer and large scale dynamics in turbulent Rayleigh-Bénard convection. *Rev. Mod. Phys.*, 81:503–537, Apr 2009.

[3] G. Ahlers, S. Grossmann, and D. Lohse. Heat transfer and large scale dynamics in turbulent Rayleigh-Bénard convection. *Reviews of modern physics*, 81(2):503, 2009.

[4] R. Benzi, F. Toschi, and R. Tripiccione. On the heat transfer in Rayleigh–Bénard systems. *Journal of statistical physics*, 93(3-4):901–918, 1998.

[5] B. Castaing, G. Gunaratne, L.P. Kadanoff, A. Libchaber, and F. Heslot. Scaling of hard thermal turbulence in Rayleigh-Bénard convection. *Journal of Fluid Mechanics*, 204(1):1–30, 1989.

[6] F. Chillà and J. Schumacher. New perspectives in turbulent Rayleigh-Bénard convection. *The European Physical Journal E*, 35(7):1–25, 2012.

[7] F. Chilla, S. Ciliberto, C. Innocenti, and E. Pampaloni. Boundary layer and scaling properties in turbulent thermal convection. *Il Nuovo Cimento D*, 15(9):1229–1249, 1993.

[8] E.S.C. Ching. *Statistics and Scaling in Turbulent Rayleigh-Bénard Convection*. Springer Singapore, 2014.

[9] M.S. Chong, A.E. Perry, and B.J. Cantwell. A general classification of three-dimensional flow fields. *Physics of Fluids*, 2:408–420, 1990.

[10] A. Cimarelli. Statistical analysis and simulation techniques in wall-bounded turbulence. *Ph.D thesis*, 2011.

[11] A. Ebert, C. Resagk, and A. Thess. Experimental study of temperature distribution and local heat flux for turbulent Rayleigh–Bénard convection of air in a long rectangular enclosure. *International Journal of Heat and Mass Transfer*, 51(17):4238–4248, 2008.

[12] National Geographic. Photos: Honeycomb clouds "communicate" rain in unison. `http://news.nationalgeographic.com/news/2010/08/photogalleries`, August 2010.

[13] S. Grossmann and D. Lohse. Scaling in thermal convection: a unifying theory. *Journal of Fluid Mechanics*, 407:27–56, 2000.

[14] R.J. Hill. Exact second-order structure-function relationships. *Journal of Fluid Mechanics*, 468:317–326, 2002.

[15] L.P. Kadanoff. Turbulent heat flow: Structures and scaling. *Physics Today*, 54(8):34–39, 2001.

[16] R.M. Kerr and J.R. Herring. Prandtl number dependence of Nusselt number in direct numerical simulations. *Journal of Fluid Mechanics*, 419:325–344, 9 2000.

[17] A.N. Kolmogorov. On the degeneration of isotropic turbulence in an incompressible viscous fluids. *Dokl. Akad. Nauk. SSSR*, 31:538–541, 1941.

[18] A.N. Kolmogorov. The local structure of turbulence in incompressible viscous fluids at very large Reynolds numbers. *Dokl. Akad. Nauk. SSSR*, 30:299–303, 1941. Reprinted in *Proc. R. Soc.* London A 434, 9–13 (1991).

[19] D. Lohse and K.-Q. Xia. Small-scale properties of turbulent Rayleigh-Bénard convection. *Annual Review of Fluid Mechanics*, 42:335–364, 2010.

[20] N. Marati, C. M. Casciola, and R. Piva. Energy cascade and spatial fluxes in wall turbulence. *Journal of Fluid Mechanics*, 521:191–215, 12 2004.

[21] J.C. McWilliams. Atmospheric and Oceanic Turbulence course notes. `http://atmos.ucla.edu/~jcm/JCM/Teaching.html`, Winter 2011.

[22] S.B. Pope. *Turbulent Flows*. Cambridge University Press, 2000.

[23] J. Ravnik, L. Škerget, and Z. Žunič. Velocity–vorticity formulation for 3D natural convection in an inclined enclosure by BEM. *International Journal of Heat and Mass Transfer*, 51(17):4517–4527, 2008.

[24] L.F. Richardson. *Weather Prediction by Numerical Process*. Cambridge Mathematical Library. Cambridge University Press, 2007.

[25] K. Sengupta and F. Mashayek. Direct Numerical Simulation of Turbulent Flows Using Spectral Methods. In *46th AIAA Aerospace Sciences Meeting and Exhibit*, Reno, Nevada, January 2008.

[26] O. Shishkina and C. Wagner. Analysis of thermal dissipation rates in turbulent Rayleigh-Bénard convection. *Journal of Fluid Mechanics*, 546:51–60, 1 2006.

[27] B.I. Shraiman and E.D. Siggia. Heat transport in high-Rayleigh-number convection. *Physical Review A*, 42(6):3650, 1990.

[28] L.N. Trefethen. *Finite Difference and Spectral Methods for Ordinary and Partial Differential Equations*. Cornell University, 1996.

[29] D.J. Tritton. Physical fluid dynamics. *Oxford, Clarendon Press, 1988, 536 p.*, 1, 1988.

[30] M. van Reeuwijk, H.J.J. Jonker, and K. Hanjalić. Wind and boundary layers in Rayleigh-Bénard convection. I. Analysis and modeling. *Phys. Rev. E*, 77:036311, Mar 2008.

[31] Q. Zhou, C. Sun, and K.-Q. Xia. Morphological Evolution of Thermal Plumes in Turbulent Rayleigh-Bénard Convection. *Phys. Rev. Lett.*, 98:074501, Feb 2007.